Journal of Applied Mechanics. Received August 11, 2022;
Accepted manuscript posted October 26, 2022. doi:10.1115/1.4056136

Influence of strain history on dynamic strain localization and stress state during high-rate tensile loading of titanium alloys: experiments, modelling and analytical methods

Govind Gour[a], Daniel Thomson[a], Karthik Ram Ramakrishanan[c], David Townsend[a], Nik Petrinic[a], Antonio Pellegrino[a1±]

[a] Department of Engineering Science, University of Oxford, Oxfordshire, OX1 3PJ, United Kingdom

[b] Department of Mechanical Engineering, University of Bristol, Bristol, United Kingdom

Abstract

The determination of the mechanical response of engineering materials subjected to high loading rates plays an important role in determining their performance and application. The high strain rate tensile response of metals is usually investigated by means of the Split Hokinson Tension Bar (SHTB) apparatus. The interpretation of the obtained results is, however, subjected to analogous stress and strain uniformity challenges present during quasi static tensile experiments. Beyond the onset of necking, strains cease to be uniform along the gauge length and localise around the necking zone. Consequently, the nominal strain rate underestimates the effective strain rate experienced by the material. The analysis of the effective strain rate and stress state beyond the onset of necking has received considerable attention in literature. Several research efforts have focused on the optimization of the geometry of specimens to be employed for the characterization of the dynamic tensile response using the SHTB. The present work investigates, systematically, the effects of strain history and adiabatic heating on the stress state during dynamic loading. A series of monotonic and various strain history experiments were conducted and analysed. The diameter evolution, effective strain rate and temperature histories were measured for all conducted experiments. Numerical simulations were carried out to examine the stress state during strain localisation and to accurately reproduce engineering and local thermos-mechanical variables. The effectiveness of existing post-necking corrections for high-rate experiments is assessed. A modified post-necking

[1±] corresponding author: antonio.pellegrino@eng.ox.ac.uk

Journal of Applied Mechanics. Received August 11, 2022;
Accepted manuscript posted October 26, 2022. doi:10.1115/1.4056136

correlation taking into account the effects of adiabatically induced thermal softening is proposed.

Keywords: Hopkinson bar, Specimen geometry, Titanium alloys, Dynamic necking, stress triaxiality

Table 1: List of symbols

a	Current minimum cross section radius
A	Cross section areas of bars
A_0	Cross section area of specimen
l_0	Original specimen gauge length
D_0	Original diameter
D (t)	Current diameter
R	Radius of curvature or necking curvature
$\varepsilon(t)$	Strain
$\dot{\varepsilon}(t)$	Strain rate
$\varepsilon_I(t)$	Incident strain history
$\varepsilon_R(t)$	Reflected strain history
$\varepsilon_T(t)$	Transmitted strain history
$\dot{\varepsilon}_0$	Reference strain rate
ε^p	Equivalent plastic strain
$\dot{\varepsilon}$	Current plastic strain rate
ε^*	$\frac{\dot{\varepsilon}}{\dot{\varepsilon}_0}$
ε_p	Engineering plastic strain
ε_N	True strain at the initiation of necking
ε_{eq}	True current equivalent strain
ε_{Pmax}	Ultimate engineering plastic strain
ε_f	Failure engineering strain
ε_{true}	True strain
$\dot{\varepsilon}_{true}$	True strain rate
$\varepsilon_{effective\ pl}$	Effective plastic strain
T	Current temperature
T_{room}	Room temperature
T_{melt}	Melting temperature

Journal of Applied Mechanics. Received August 11, 2022;
Accepted manuscript posted October 26, 2022. doi:10.1115/1.4056136

$\sigma(t)$	Dynamic stress
σ_{true}	True stress
σ_{flow},σ_{eq}	Equivalent or von Mises stress or Flow stress
σ_{eng}	Engineering stress
σ_{eq_avg}	True equivalent stress averaged over the minimum cross section
(σ_x)	Axial stresses
(σ_r)	Radial stress
(σ_h)	Hoop stress
$(\frac{r}{a})$	Radial coordinates (neck center to necking outer radius)

1. Introduction

Titanium alloys have been a popular choice in various engineering applications, namely defense, aerospace, and automotive, credit to their excellent strength to density ratio coupled with superior corrosion resistance and durability. The well-balanced strength and ductility have made Ti6Al4V one of the most versatile titanium alloys, a composition that finds application in various engineering sectors. Generally, this class of materials is strain rate dependent and requires a careful assessment of their processing history, surface texture and grain size [1, 2]. The recent research in material science and metallurgy pushed towards the development of novel ductile titanium alloys such as Ti0.7Al4V and Ti1Al4V [3-5] for impact containment applications, among the others. It is thus envisaged that reduced strength and increased ductility will provide improved performance in such applications, whilst significantly reducing manufacturing costs. Recent studies showed that a new titanium alloy, Ti0.7Al4V, benefits from significantly reduced flow stress during forming [6].These ductile alloys are capable of dissipating considerable energy during deformation and failure and their applications include, but are not exclusive to, blade containment in jet engines, impact of foreign objects, ice injection, crashworthiness, etc. The accurate prediction of the mechanical response of the material under large deformation requires the rigorous evaluation of its true equivalent stress and equivalent strain characteristic.

Typically, the equivalent stress and equivalent strains are estimated by means of standard uniaxial tensile experimentation using either cylindrical smooth round or flat specimens. Before the onset of necking in when the deformation is uniform, the logarithmic form provides a reasonably good description of true stress and true strain in the material. However, beyond

the onset of necking the deformation ceases to be uniform along the gauge length of specimen. In fact, after necking initiates, strain localizes around the minimum cross section and cannot be related anymore to the gauge length. Moreover, the stresses in the specimen are no longer uniform and a triaxial stress state develops in the necked region. As a result, the computation of the stresses and strains using their nominal or logarithmic form poorly approximates the true stress and true strain in the necked region of the specimen [7, 8]. Therefore, the identification of accurate equivalent stress-strain characteristics in the post-necking regime is crucial for the accuracy of the measured mechanical properties.

The Split Hopkinson pressure bar is commonly used to acquire the high strain rate mechanical response in the range of 10^2 s^{-1} to 10^4 s^{-1}. The displacements and forces on the specimen can be determined from the recorded strain gauge signals using one-dimensional wave analysis and used to calculate nominal stresses and strains within the specimen. A detailed description about the theory and basic formulation of this apparatus can be found in [9]. The calculation of the true stress and true strain in the post-necking phase is possible only if the diameter evolution of the cross section is accurately measured, for example using high-speed imaging or alternative equivalent methods such as laser profiling. [10].

During dynamic tensile testing, homogeneous strains are limited to the early stage of deformation and are usually followed by the onset of necking (strain localization). In the necked region, the rapid increase of plastic strains generally causes the temperature to rise. Therefore, it is expected to observe large thermal gradients in the necked region relative to the rest of the gauge length. Moreover, the estimation of the overall temperature rise is an important aspect to model for impact events, where adiabatic heating can significantly soften the material response. In addition, particularly when strong and ductile materials undergo large deformation at high rate, a large amount of plastic work is dissipated in a short time, resulting in heat generation and non-isothermal conditions. Experiments conducted using an infra-red detector on commercially pure titanium reported that almost the total amount of plastic work done during the dynamic deformation is converted into heat [11]. Macdougall and Harding [12, 13] utilized infrared radiometry to quantify the fraction of plastic work converted into heat and evaluate the Taylor-Quinney coefficient. They conducted high-rate testing on tensile and torsion specimens made of Ti6Al4V and concluded that the conversion factor increases with increasing plastic strain. They reported that the value of β ranges from 0.5 to 0.9 and from 0.5 to 1.0 for tension and torsion testing, respectively. Noble et. [14] used a thermal imaging

camera and found that the peak temperature rise due to adiabatic heating can reach approximately 300C for iron tensile specimens, which is sufficient to influence considerably the mechanical response of metals. Ranc et al. [15] showed that the temperature increase comprises of two stages; a quasi linear increase occurring when the flow stress is almost constant, and a rapid increase of temperature when the flow stress begins to drop associated with the formation of adiabatic shear bands. Several researchers have measured the real-time surface temperature of steel, aluminium, Inconel, and titanium alloys [16-22] using high-speed IRT or similar techniques. The dependence of the Taylor-Quinney coefficient on the dynamic loading mode and on the investigated material was examined in [21] using a high-speed infrared radiation detector to measure the temperature evolution on the tested specimens. The concurrent effects of dynamic strain localization and adiabatic heating were recently assessed in [23].

The use of conventional manufacturing processes such as sheet forming, ring rolling, or cross rolling induces a certain amount of strain history on the materials. It is therefore interesting to investigate the effect of pre-strain on dynamic strain localisation and stress state. Wu et al [24] investigated the effect of pre-strain on microstructure and tensile properties of Ti-6Al-4V at elevated temperature. It was found that the level of pre-strain affects the hot forming performance of Ti6Al4V. Various investigations examined the microstructural evolution and deformation mechanism with pre-strain history at low rate loading [24-26]. A number of studies assessed the effect of plastic pre-strain on high cycle fatigue and fatigue crack growth behaviour [27, 28]. The results suggest that plastic pre-strain enhances fatigue life and delays the crack growth rate.

To the authors' knowledge, there is no previous investigation on the influence of pre-strain on necking evolution and stress triaxiality during high rate tensile deformation. Additionally, it is important to assess the effect of adiabatic heating on the stress state within the necking area. An extensive series of quasi-static pre-strain experiments followed by high strain rate tensile deformation constitutes the experimental baseline to determine the temperature history in the necked area of the specimen.

The present research work investigates, systematically, the effects of strain history on the effective strain rate, thermal softening and stress state during dynamic tensile loading in Ti6Al4V. A series of monotonic and quasi-static pre-strain experiments followed by high strain rate loading are conducted and analysed. Many researchers have investigated the effect of

Journal of Applied Mechanics. Received August 11, 2022;
Accepted manuscript posted October 26, 2022. doi:10.1115/1.4056136

triaxiality in post-necking and corrected true curves into equivalent stress-strain curves [29-37]. However, no systematic investigation to understand the application and reliability of these corrections for high-rate and strain rate history experiments has been found. With this work we present a systematic study assessing the validity of post necking corrections for high rate experiments. The high strain rate, pre-strain history experiments and their corresponding simulations demonstrate that the temperature rise consequent to adiabatic heating affects the stress distribution in the necking area. Finally, a modified post-necking correction, taking into account the parameters related to adiabatic heating is proposed and verified.

2. Experimental setup and material specification

This section presents the key details of specimen design, manufacturing and of the experimental set-ups used for quasi-static, pre-straining and high strain rate loading experiments.

2.1 Specimen geometry and preparation

The tensile specimen geometry was selected based on the previous research conducted at Impact engineering lab at University of Oxford. A smooth cylindrical specimen with 8 mm gauge length and 3 mm diameter was used in quasi-static, high strain rate and strain history experimentation as illustrated in Figure 1.

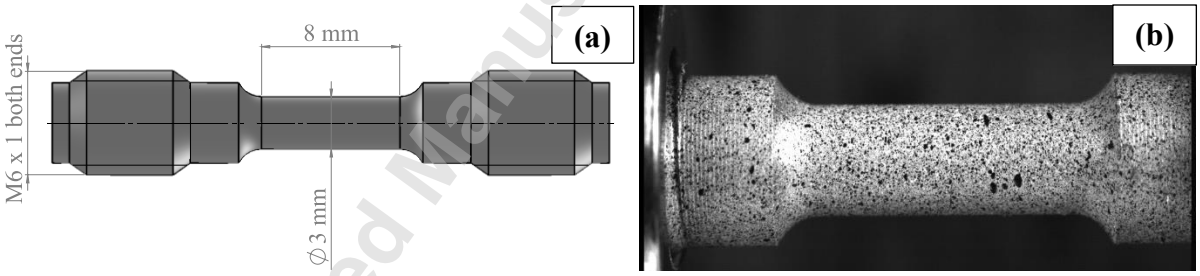

Figure 1:(a) geometrical description of the tensile specimen and (b) example of speckle pattern for DIC analysis.

Speckle patterns with a white background and black dots were applied on every specimen using an appropriate airbrush, thus enabling the full field strain analysis on the specimen by means of the digital image correlation (DIC) technique. In the present study, the commercially available GOM-Aramis® was used to investigate the strain field at low and high rates of deformation. The quality of the speckle pattern was assessed using the mean intensity gradient (MIG) for the region of interest as a metric [38]. The MIG has been set as a standard value to

assess the quality of the speckle pattern and has been reported as an important parameter for DIC analysis. Pan et al. [39] created various speckle patterns with MIG varying from 09 to 35 and presented an extensive comparison of mean bias and standard deviation error. The conclusion reports that a MIG value of 20 or higher is a good indicator for good DIC analysis. The quality of the speckle patterns was investigated on various samples. The average value of the MIG was found to be around 30, higher than the minimum recommended value.

2.2 Specimen Material

The tensile specimens were manufactured from a commercial cross-rolled plate to keep any directionality in the mechanical response negligible. The details of chemical composition and quasi-static mechanical properties are tabulated in Table **2**.

Table 2: Chemical composition and basic mechanical properties of the Ti-6Al-4V used in this study.

Weight (%)	N	C	H	Fe	O	Al	V
Max	*0.05*	*0.08*	*0.015*	*0.40*	*0.20*	*6.75*	*4.5*

Density (g/cm3)	Young's modulus (GPa)	UTS (GPa)	Failure ε_{eng} %
4.419	110	895	17-19

2.3 Quasi-static experimental setup

A screw-driven mechanical test machine Zwick-050 with 20kN load cell was used to determine the quasi-static response and to introduce pre-strain in the pristine samples. The pre-straining set-up included a non-contact video extensometer (IMT-CONTR-VG5-ADV®[2]) controlling strains in real time with high accuracy equipped with a 1936×1216 resolution camera (IM-CAM-037[2]) and a magnification lens (MT018) with a focal length of 186 mm. Once the desired strain was achieved, the load was removed to neutralize the reaction forces. In addition a 2456×2054 pixel iDS[1] UEye USB 3.0 camera, equipped with a low distortion lens was used for image acquisition and subsequent full-field DIC strain analysis, see Figure **2** (a). Different quasi-static pre-strain levels, namely 6%, 10%, and 14% engineering total strain (ε_{eng}), as

[2] Imetrum Limited, The Courtyard, Wraxall Hill, Wraxall, Bristol, BS48 1NA, United Kingdom

Journal of Applied Mechanics. Received August 11, 2022;
Accepted manuscript posted October 26, 2022. doi:10.1115/1.4056136

illustrated in Figure **2**(b), were prescribed for the subsequent high-rate of deformation experiments.

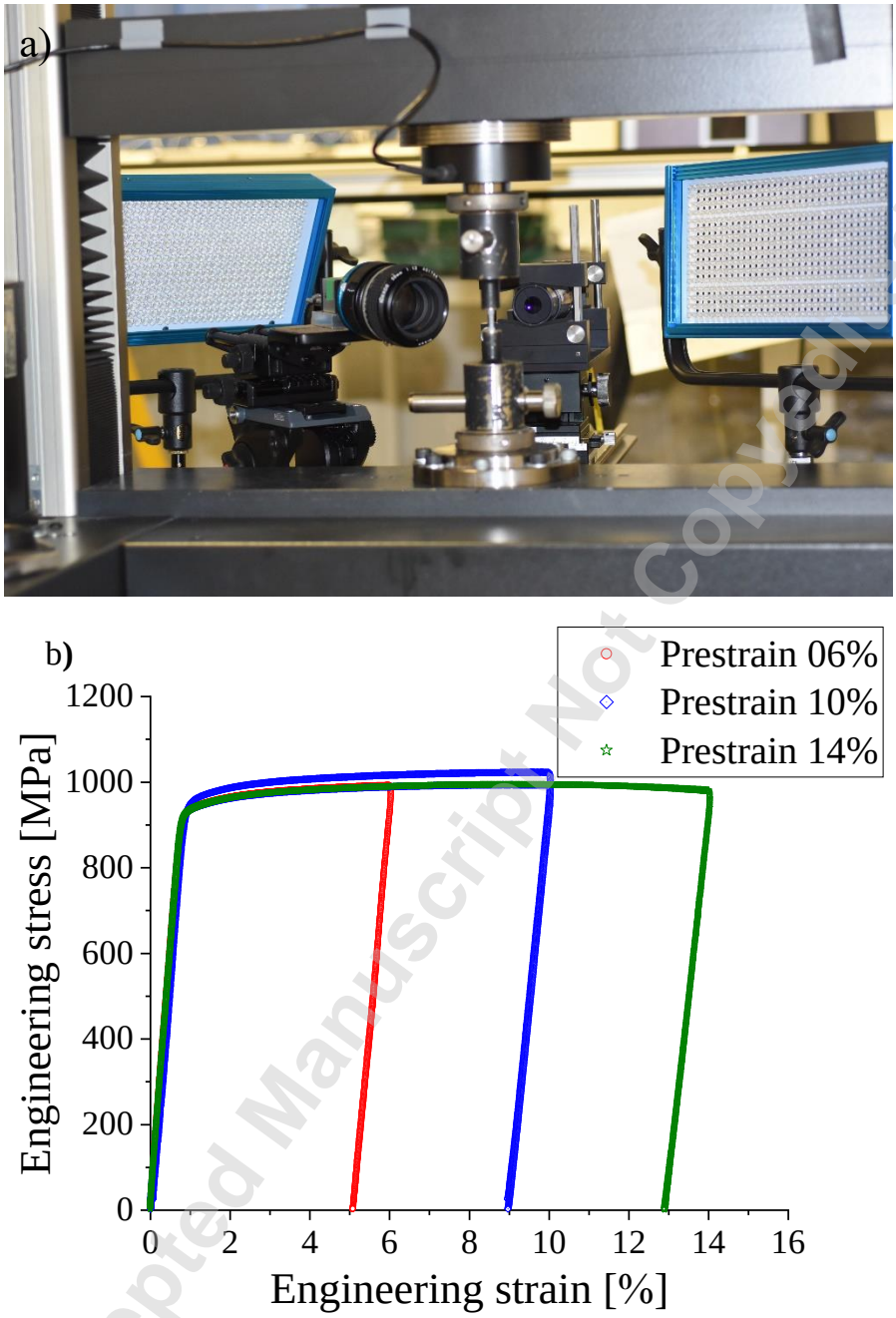

Figure 2: (a) quasi-static loading, strain control and imaging setup (b) example of pre-straining of a Ti6Al4V specimen.

It is noted that, although the applied pre-strains have been labelled as 6%, 10% and 14%, the amount of plastic strain within the gauge length of the samples after unloading is less for each of the pre-strain levels. This is because the material unloads elastically at the end of the pre-straining stage. Therefore, the deformation in the material is reduced by the elastic strain

Journal of Applied Mechanics. Received August 11, 2022;
Accepted manuscript posted October 26, 2022. doi:10.1115/1.4056136

corresponding to the stress exerted prior to unloading.

2.4 High-rate experimental setup

The dynamic experiments on pristine and pre-strained specimens were carried out using an in-house developed Split Tensile Hopkinson Bar (SHTB) apparatus, represented schematically in Figure 3. Detailed information on the apparatus can be found in [40]. The input and output bars were made of titanium grade 5 with a solid cross section of 10 mm in diameter and a length of 2700 mm. Various striker lengths from 500 mm to 2500 mm can be used to achieve strain rate ranging from 300 s^{-1} to 3000 s^{-1}. The longer strikers enables a longer duration of the stress pulse, which is useful to deform and fail samples even when the strain-rate is relatively low. The high-rate experiments were recorded using a Specialised Imaging Kirana high speed camera operating at 0.5 million frames per second. The acquired images were processed using the commercial DIC software GOM Aramis®[3] for the accurate measurements of elongation and diametrical contraction in the sample, analogously to what was done for the quasi-static experiments.

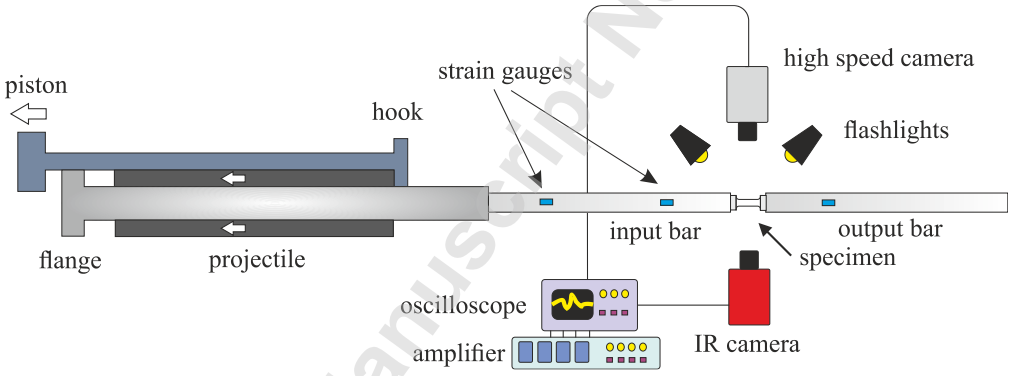

Figure 3: schematic of the Split Hopkinson Tension Bar apparatus

When using the short projectile the incident and reflected stress pulses do not superimpose during the experiments. Hence, stress and strain histories can be calculated using the classic SHB analysis, reported in Gray et al. [9]. Dynamic stress (t) , strain $\varepsilon(t)$ and strain rate $\dot{\varepsilon}(t)$ can be evaluated at any time during the transient experiment using the following formulation:

$$\sigma(t) = \frac{EA}{A_0}\,\varepsilon_T(t) \qquad (1)$$

[3] GOM UK, Siskin Parkway East, 14, The Cobalt Centre, Coventry, UK

Journal of Applied Mechanics. Received August 11, 2022;
Accepted manuscript posted October 26, 2022. doi:10.1115/1.4056136

$$\varepsilon(t) = \frac{-2c}{l_0} \int_0^t \varepsilon_R(t)\, d\tau \quad (2)$$

$$\dot{\varepsilon}(t) = \frac{-2C}{l_0}\, \varepsilon_R(t) \quad (3)$$

$$\varepsilon_I(t) + \varepsilon_R(t) = \varepsilon_T(t) \quad (4)$$

Where E is the young's modulus of the bars, A and A_0 are the cross-section areas of the bars and specimen, respectively; c represents the longitudinal elastic wave propagation velocity of the input/output bars, l_0 is the original specimen gauge length. $\varepsilon_I(t)$, $\varepsilon_R(t)$, $\varepsilon_T(t)$ represent incident, reflected and transmitted strain histories recorded in incident and transmitted bars. In addition to the high-speed camera, a Telops FAST-IR-M3K infra-red camera was employed to observe the temperature history during quasi-static and high-rate mechanical tests. It features a spatial resolution of 320×256 pixels with a spectral range of 1.5 µm to 5.4 µm. An integration time of approximately 5µs and a frame rate of 100000 fps were used during high rate experiments. However, these settings resulted in a resolution trade-off and images were acquired in sub-window mode of 64 x 4 pixels. For the quasi-static tests, the frame rate used was 1 Hz, the integration time was 50µs and the resolution was 64 × 64 pixels. The triggering of the infrared camera and of the high speed camera was achieved using the rising edge of the incident pulse to ensure the temporal synchronization of load, strain and temperature measurements. Table 3 summarizes the experiments conducted in this study.

Table 3: summary of the experiments conducted in the current study.

Material : Ti-6Al-4V	Strain rate	Repetition
Pristine - Monotonic	1800 s^{-1} – 2100 s^{-1}	7
Quasi-static	10^{-3} s^{-1}	4
<u>Pre-strain</u>		
06	1800 s^{-1} – 2100 s^{-1}	7

10	1800 s^{-1} – 2100 s^{-1}	8
14	1800 s^{-1} – 2100 s^{-1}	7

3. Results and discussion

This section summarizes the experimental results obtained from, quasi-static, high rate monotonic and strain rate jump experiments with different pre-strain levels. Firstly, the achievement of dynamic equilibrium conditions during high-rate experiments is assessed. Following, the mechanical responses of pristine and pre-strained Ti-6Al-4V samples, as well as the time histories of the necking diameter are presented. Finally, the temperature increase during high-rate testing for each loading case is presented.

3.1 Dynamic response and effect of strain history on dynamic strain localisation of Ti-6Al-4V

Dynamic equilibrium conditions [9] have been verified for all experiments to assess the validity of the experimental results presented in this section. Figure **4** illustrates the comparison of the force histories measured on the sample at the interfaces with incident and transmitted bars, during a representative experiment. It is evident that dynamic equilibrium conditions were achieved and that the strain rate is substantially stable during loading. This conditions were attained for each of the reported experiments.

Journal of Applied Mechanics. Received August 11, 2022;
Accepted manuscript posted October 26, 2022. doi:10.1115/1.4056136

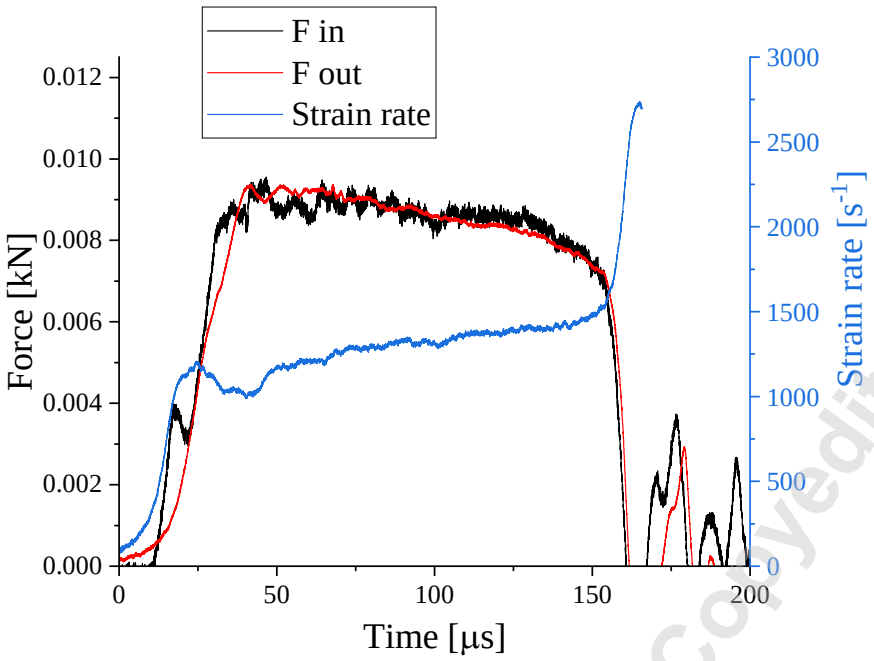

Figure 4: dynamic equilibrium during a representative Split-Hopkinson Tension Bar experiment.

During plastic deformation, beyond necking, the deformation ceases to be uniform along the gauge length and the computation of the true stresses and strains obtained using their logarithmic form constitutes an inaccurate approximation of the real material behaviour, especially in the localized region of the specimen. Moreover, beyond the onset of necking, strain becomes localized around the minimum cross section and cannot be related anymore to the gauge length. A complete evaluation of true stress-strain characteristic can only be obtained if the diameter of the necking cross section radius is monitored accurately during loading and the following equations are used:

$$\varepsilon_{true}(t) = 2\ ln\left(\frac{D_0}{D(t)}\right) \tag{5}$$

$$\sigma_{true}(t) = \frac{4F(t)}{\pi D(t)^2} \tag{6}$$

$$\dot{\varepsilon}_{true}(t) = \frac{d}{dt}\left[2\ ln\left(\frac{D_0}{D(t)}\right)\right] \tag{7}$$

Where $\varepsilon_{true}(t)$ and $\dot{\varepsilon}_{true}(t)$ represent the true strain and true strain rate histories, $\sigma_{true}(t)$ is the evolution of the true stress over time, D_0 is the initial diameter of the specimen and D(t) is

Journal of Applied Mechanics. Received August 11, 2022;
Accepted manuscript posted October 26, 2022. doi:10.1115/1.4056136

the current diameter of the necking cross section.

The nominal strain rate underestimates the effective strain rate experienced by the materials after the strain localization. This is particularly evident for ductile metal alloys. The effective strain rate can be evaluated by differentiating the true strain with respect to the time interval. Generally, the effective strain rate can be much higher in magnitude than the nominal strain rate [7] . With the aid of high-speed imaging techniques, it is possible to measure accurately the diameter evolution during dynamic experiments. By knowing the time associated with the captured images, it is possible to infer an accurate true strain rate history.

The high strain rate engineering and true stress-strain characteristics measured during dynamic experiments on pristine samples and on samples pre-strained quasi statically at 6%, 10% and 14% of their initial gauge length are illustrated in Figure **5**. The alloy shows an evident rate dependent yield stress, increasing from 910 MPa at a strain rate equal to 0.0008 s^{-1} to 1250 MPa at strain rates of approximately 2000 s^{-1}. Compared to the pristine material, the specimens pre-strained at 6% and 10% present a slightly lower failure engineering strain (ε_f) with average values of ε_f equal to 18% and 19% respectively, compared to an average ε_f equal to 20% measured on pristine samples. The effect of the strain history on the strain to failure of Ti6Al4V is even more noticeable when analysing the true stress-true strain curves reported in Figure **5** (b), with an average true strain to failure equal to 0.67 for monotonic high rate experiments, compared to values equal to 0.55, 0.44, and 0.47 measured on samples pre-strained at 6%, 10% and 14% of their initial gauge length.

Journal of Applied Mechanics. Received August 11, 2022;
Accepted manuscript posted October 26, 2022. doi:10.1115/1.4056136

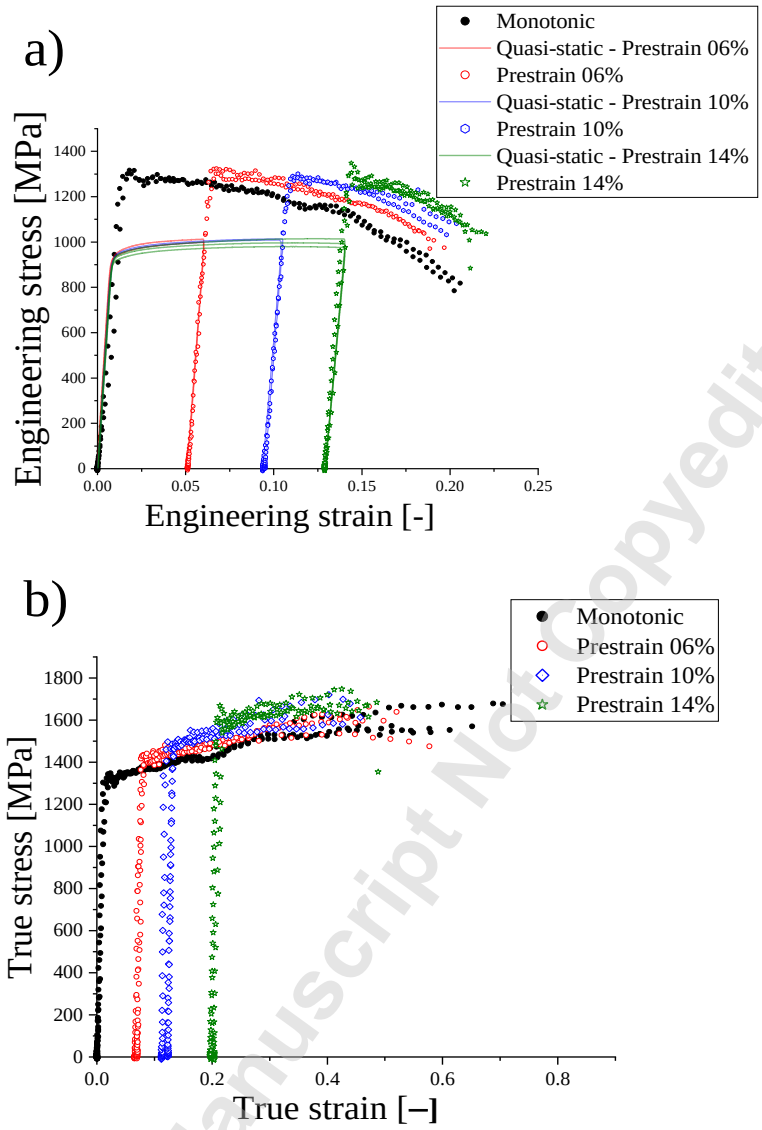

Figure 5: a) engineering stress-strain characteristics of monotonic and pre-strained Ti-6Al-4V specimens; quasi static pre-strain and dynamic loading b) dynamic true stress–strain response of monotonic and pre-strained Ti-6Al-4V specimens.

It is also apparent that there is a difference in the thermal softening behavior for the pre-strain Ti6Al4V alloys. When the samples are pre-strained at 10% and 14% and later tested using the SHTB, they showed a larger yield point and a higher flow stress compared to the pristine specimen response. This is explained by considering the effects of high-rate plastic deformations on the temperature of the material and, consequently, on its flow stress. High-rate experiments, as plastic deformation occur in very short time, do not allow for any significant

Journal of Applied Mechanics. Received August 11, 2022;
Accepted manuscript posted October 26, 2022. doi:10.1115/1.4056136

heat to be exchanged with the surrounding environment [11, 41]. This results in an increase of temperature within the sample, proportional to the plastic work per unit of volume dissipated in the material (the area under the true stress-strain curve), commonly referred as adiabatic heating. On the contrary, the heating at low strain rates is very small [42]. During dynamic experiments on pristine samples the total amount of plastic work is dissipated in adiabatic conditions, while on pre-strained samples part of the plastic work is dissipated at quasi-static rates of strain. The temperature increase in the material is therefore expected to be higher during dynamic experiments on pristine samples. Consequently, as the mechanical response of materials is generally affected by the temperature, the softening on monotonic experiments is higher than on pre-strained samples.

Figure 6 illustrates the diameter contraction as a function of the engineering strain and its derivative with respect to the same variable. It is clear that the diameter contraction is affected by the amount of pre-strain imposed on the samples, as its final value prior to failure appears to be more significant on pristine samples and to gradually decrease for increasing levels of pre-strains (Figure 6 (a)). Additionally, the diameter of the pre-deformed samples appears to reduce more gradually during the initial phases of high-rate loading, a feature missing in the diameter evolution of pristine samples. The diameter contraction of 14% pre-strained samples during the early stages of dynamic loading is illustrated in detail in the zoom plot in Figure 6a. It is observable that the necking diameter reduces moderately until engineering strains between 0.145 and 0.15 and then more rapidly beyond these strains. A similar behavior is observed on 6% and 10% pre-strained samples.

This is also confirmed by Figure 6 (b), which illustrates the envelopes of the rate of contraction of the diameter with respect to the engineering strain, together with the corresponding average values for all levels of pre-strain. The rate of reduction of the necking diameter appears to be higher for monotonic experiments on pristine samples and it is reduced for higher levels of pre-strain. The above effects are ascribed to the larger amount of plastic work dissipated into heat during high-rate experiments on samples characterised by lower pre-strain. The amount of adiabatic heating generated during plastic deformation is expected to affect the strain localisation in the necking area and, in turn, the stress state around the minimum diameter of the sample.

Journal of Applied Mechanics. Received August 11, 2022;
Accepted manuscript posted October 26, 2022. doi:10.1115/1.4056136

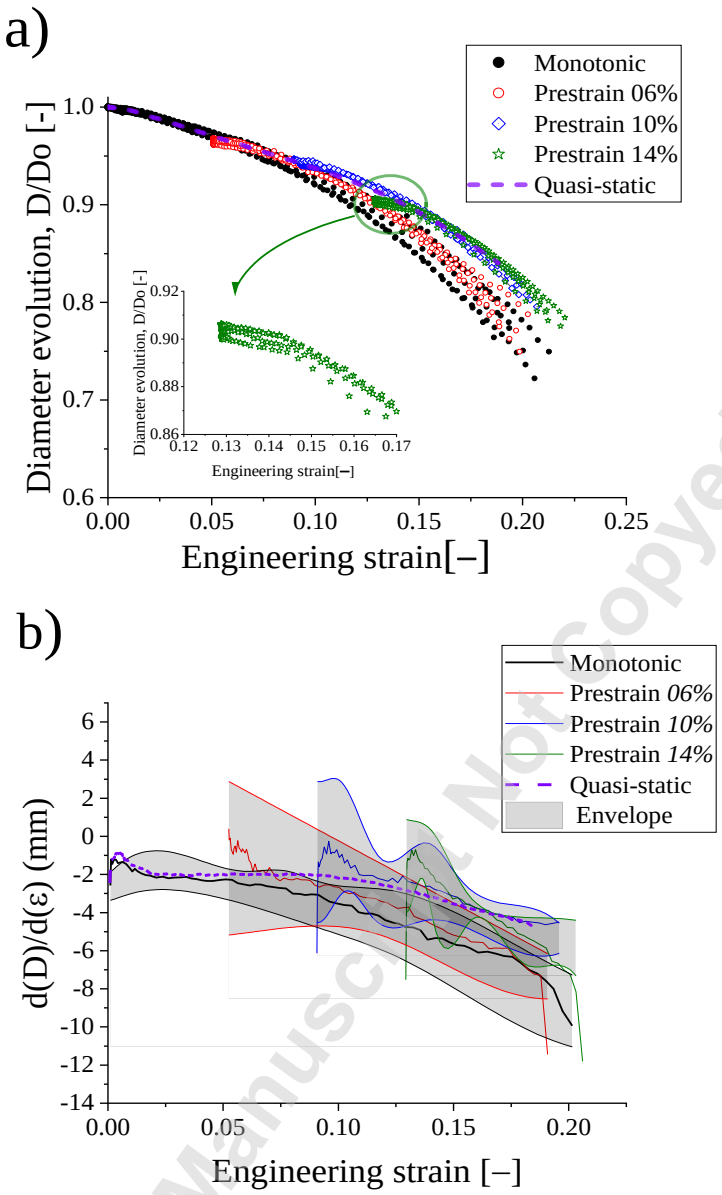

Figure 6: a) diameter contraction of monotonic and pre-strained Ti6Al4V samples, b) rate of diameter contraction, envelopes and average values for all levels of initial pre-strain.

3.2 Measurement of Temperature rise

A high-speed infrared camera (Telops FAST-IR-3K) was used to monitor the temperature change during the mechanical testing at quasi-static and high loading rates, as shown in Figure **7** (a). The IR camera considers the target as a black body with emissivity of one while monitoring the temperature change. Therefore, it is necessary to examine the emissivity to account for the influence of the speckle pattern on the specimen. A conversion factor between

Journal of Applied Mechanics. Received August 11, 2022;
Accepted manuscript posted October 26, 2022. doi:10.1115/1.4056136

radiometric and surface temperature was estimated via the following procedure: (a) the sample was heated slowly in a controlled environmental chamber until reaching a stabilized temperature, (b) a K-type thermocouple, connected to a temperature logger, was spot welded onto the surface of the sample, and (c) the temperature change was monitored during the cooling of the specimen. A linear fit was used to convert the radiometric temperature to surface temperature and the surface emissivity was found to be between 0.91 and 0.96 for the matt paint applied on the surface of the titanium samples. The calibration was repeated three times in similar testing conditions and the average full field radiometric temperature of the specimen was compared with the surface temperature measured by the thermocouple.

Ti6Al4V is characterised by low thermal conductivity, which restrains the dissipation of the heat generated during the plastic deformation rapidly into the environment [43]. It is, therefore, reasonable to believe that the temperature increment caused by adiabatic heating in the material increases its ductility, exacerbating the rate of reduction of the diameter in the necking area, particularly at relatively large nominal strains. The Taylor-Quinney coefficient could therefore be determined by means of reverse engineering procedures, using material models able to accurately represent strain localization in ductile alloys [4].

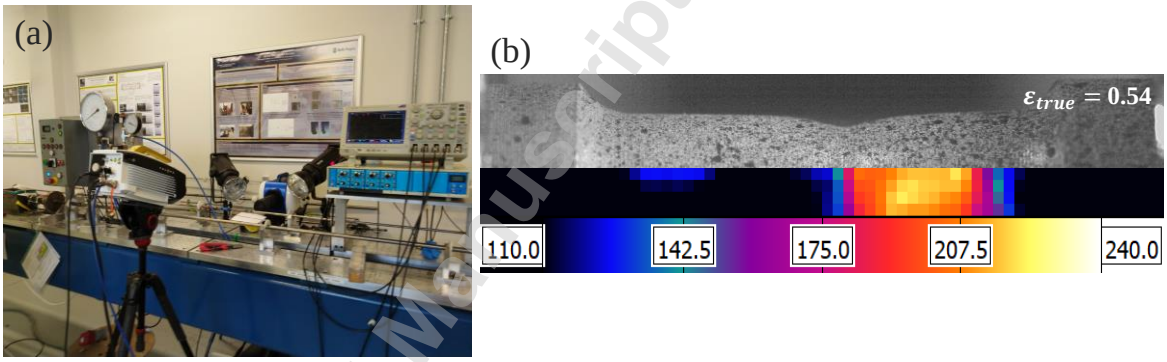

Figure 7: detail of the experimental setup: (a) Split-Hopkinson Tensile Bar equipped with infrared thermal camera and high-speed camera, (b) example of the temperature distribution during dynamic strain localisation.

Prior to every mechanical test, it was ensured that the centre of the specimen remains in the field of view of the infrared camera to avoid any influences on the measurements. The full field measurement of the thermal camera avoids the limitation of using thermocouple for measuring the adiabatic heating temperature. Despite the reduced resolution necessitated by the high speed acquisition, the setup pictures show that the entire length of the tensile specimen is captured in the 64 pixels of the thermal camera. The width of 4 pixels also covers the entire diameter of the specimen and this allows the measurement of the temperature at the necking zone without

a priori knowledge of its location. Initial experiments of the high strain rate tests of Ti64 samples showed that the temperature in this zone exceeded the 176 °C limit of the calibration range of the Telops camera. A calibration file with temperature ranging from 110 °C to 378 °C was used instead for all the tests. Since the current study focuses on the identification of the effect of pre-straining on the stress state in the necked section, it was essential to find out the overall peak temperature rise during high-rate testing for various pre-strain levels. This calibration range meant that it was not possible to measure the temperature evolution from room temperature and the measurement focused on the necking phase.

Figure **8** illustrates the experimental results for two representative experiments where the temperature evolution is observed for pristine and pre-deformed tensile specimens with pre-strain level equal to 10% engineering strain. It can be seen that the temperature reaches approximately 220 °C for the pristine case, while for the pre-strained sample the peak temperature is in the region of 195 °C.

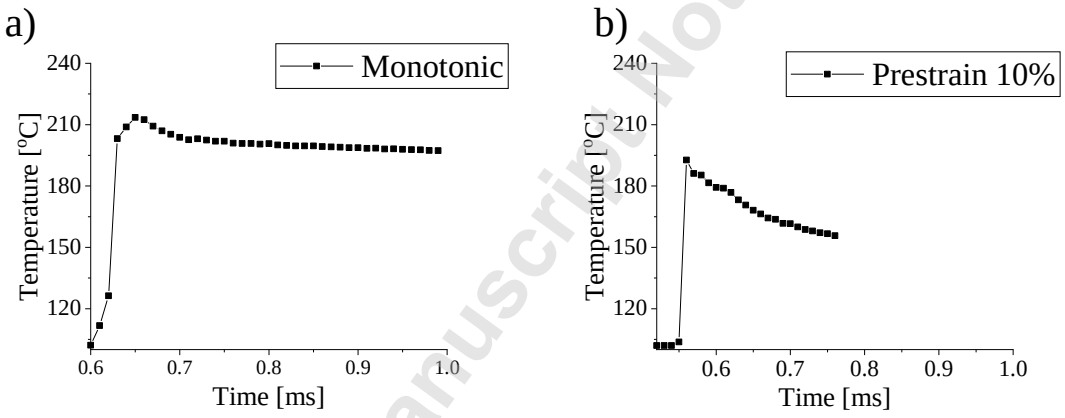

Figure 8: temperature evolution during high rate experiments: (a) Pristine Ti-6Al4V specimen and (b) 10% Pre-strained Ti-6Al4V specimen.

The effect of the pre-strain on the necked region of the sample can be further analysed synchronising the infrared thermal images with the images captured by the high speed camera (Figure 9). It is evident that the overall temperature rise appears to be less significant on the 10% pre-strained sample compared to the pristine specimen. Correspondingly, the strain localisation around the necking region also appears to be more pronounced on the pristine sample.

Journal of Applied Mechanics. Received August 11, 2022;
Accepted manuscript posted October 26, 2022. doi:10.1115/1.4056136

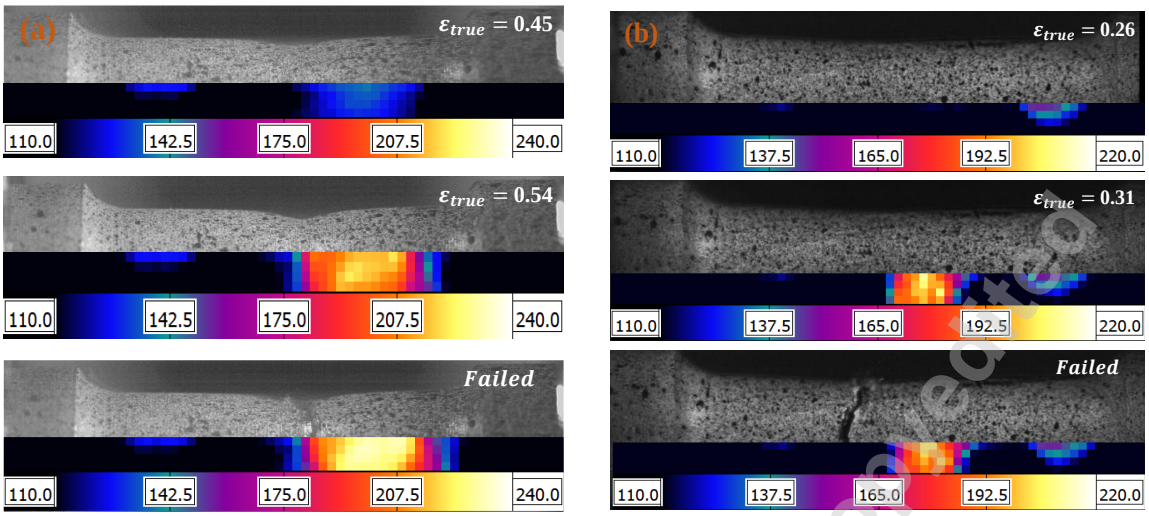

Figure 9: full field radiometric temperature profile and deformation of Ti6Al4V tensile samples: (a) high rate experiment on pristine sample and (b) high rate experiment on pre-strained sample, 10% engineering pre-strain.

Figure **10** presents the peak temperature as a function of the level of pre-strain for all experiments presented in this study. By observing the trend, it is possible to conclude that the overall temperature rise during high rate experiments is inversely proportional to the imposed level of pre-strain. This is because the short duration of high-rate experiments does not allow for any significant heat to be transferred to the surrounding environment, resulting in an increase of temperature proportional to the work dissipated during plastic deformation. Conversely, this temperature increment results negligible during quasi-static experiments [42]. On pre-strained samples a portion of the plastic work, proportional to the level of pre-strain, is done quasi statically, hence the lower measured peak temperature. The above considerations rationalise the trend illustrated in Figure **10**.

Journal of Applied Mechanics. Received August 11, 2022;
Accepted manuscript posted October 26, 2022. doi:10.1115/1.4056136

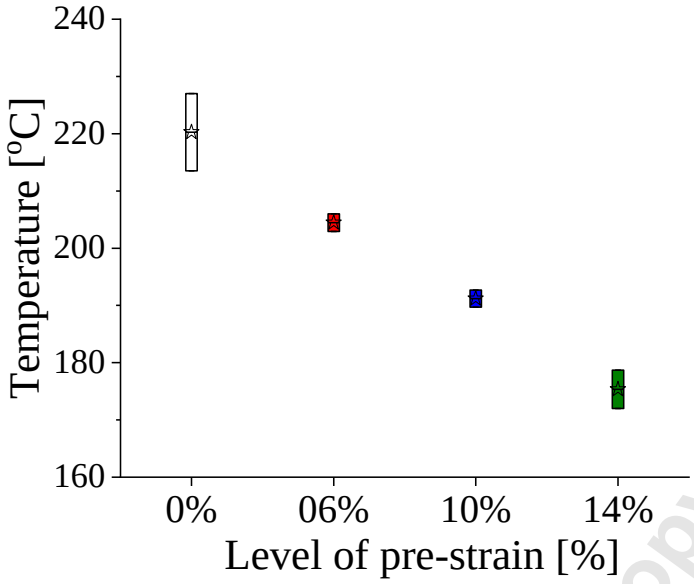

Figure 10: peak temperature during high-rate tensile experiments for various levels of pre-strain: average values and scatter.

4. Numerical modelling

The axial stresses and necking diameter evolution under different levels of pre-strain were measured experimentally by means of stress wave analysis and high speed photography. However it is not possible to measure experimentally the entire stress state around the necking area and its temporal evolution during the dynamic straining, as these also require the components of hoop and radial stress. Hence, numerical modelling techniques are essential to investigate further the influence of strain history on the dynamic strain location. The relevant details are outlined in the following sections.

4.1 Model development

The numerical analysis was carried out using the commercially available explicit solver LS-DYNA®. To reduce the computational cost, the experimental set-up was simplified into a simple tensile specimen geometry using appropriate boundary conditions. The specimen was meshed using single point integration 8-node hexahedral solid elements. These elements are a popular choice in modelling impact and large deformation problems [44].One end of the specimen was constrained using fully fixed boundary conditions whilst the boundary conditions at the other end correspond to the particle velocities and displacement histories measured during the experiments by means of image analysis of the recorded pictures.

Following a mesh sensitivity analysis, a discretization with elements of size varying from

Journal of Applied Mechanics. Received August 11, 2022;
Accepted manuscript posted October 26, 2022. doi:10.1115/1.4056136

approximately 0.29 mm to approximately 0.2 mm from the ends to the centre of the specimen was selected. Figure 11 illustrates the details of mesh and boundary conditions for both the quasi-static pre-strain and the subsequent high-rate loading. It is noted that displacement boundary conditions were used to simulate the quasi-static preliminary deformation while velocity boundary conditions were used to simulate the dynamic loading.

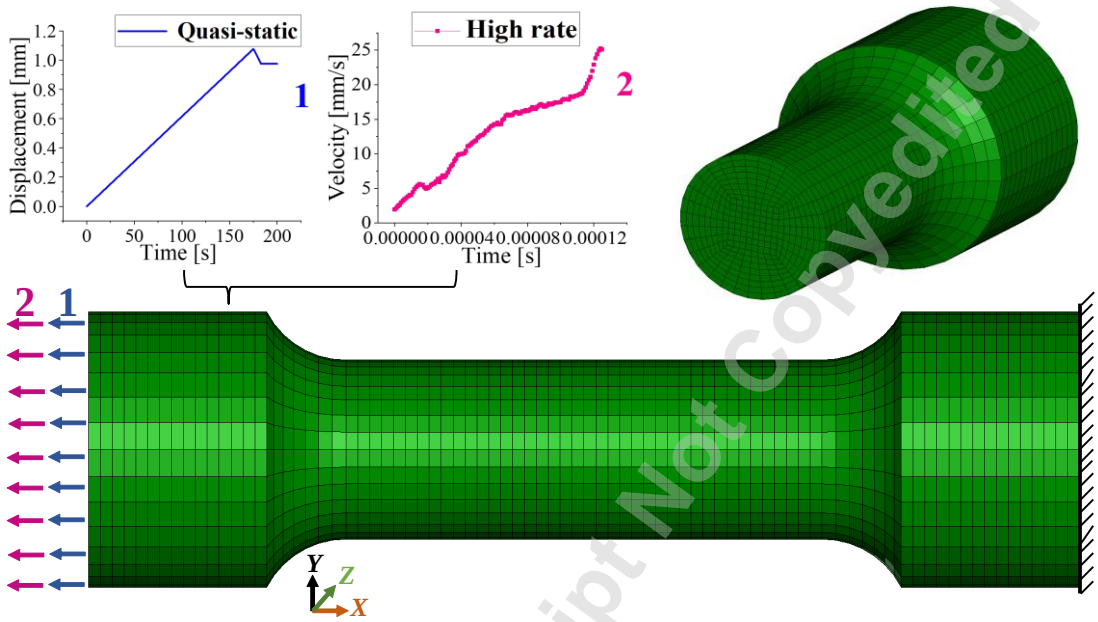

Figure 11: schematic illustration of the tensile numerical model with corresponding displacement and velocity boundary conditions.

An appropriate amount of mass scaling was used to obtain a reasonable computation time while ensuring negligible kinetic energy to avoid any inertial effects on the results. The numerical model of pre-deformation and dynamic loading experiments comprises of the following steps:(a) the specimens are loaded using displacement boundary conditions to obtain the desired amount of preliminary strain (b) Once the desired pre-strain level is achieved, the specimens are unloaded until the resultant forces reduce to zero, (c) the pre-strained specimens, retaining information on plastic strains, stress states and internal state variables are loaded dynamically using the particle velocities boundary conditions measured during high rate experiments. Thermal boundary conditions are applied to both ends of the specimen. The numerical problem was set-up using a fully coupled thermal-stress analysis in LSDYNA explicit solver. The thermal time increment for QS and HR were set to 1 s and 1μs, respectively.

4.2 Material modelling of Ti-6Al-4V

The mechanical response of the sample was modelled using the empirical formulation proposed by Gordon R Johnson and William H Cook. [45]. The Johnson-Cook (J-C) model is based on von Mises plasticity and describes the dependency of the plastic flow stress on equivalent plastic strain, strain rate and temperature. The classic form of the -JC model is multiplicative and isolates the aforementioned effects on the flow stress σ as it follows:

$$\sigma = [A + B(\varepsilon^p)^n]\left[1 + Cln\,(\dot{\varepsilon^*})\right]\left[1 - \left(\frac{T - T_{room}}{T_{melt} - T_{room}}\right)^*\right]^m \quad (8)$$

Where A, B, C, n and m are constants, ε^p is the equivalent plastic strain, $\dot{\varepsilon}$ is the current plastic strain rate, $\dot{\varepsilon}_0$ is the reference strain rate. T_{melt} is the melting temperature of the material and T_{room} is the ambient room temperature. It is well known that, the energy dissipated during plastic deformation of metallic materials is predominantly converted into heat. This can lead to a substantial rise in temperature if there is no sufficient time for the heat to dissipate, as it occurs under dynamic strain rates. The consequent non-isothermal conditions result in softening of the flow stress and can, for some materials, lead to phase transformation [46]. The fraction of plastic work converted into heat is usually quantified using the Taylor-Quinney coefficient [47, 48]. The relationship between the plastic work dissipated per unit of volume and the corresponding amount of generated heat is therefore given by:

$$\beta_{int}\int_0^{\alpha}\sigma\, d\varepsilon_P = \rho c_p \Delta T \quad (9)$$

Where ρ is the material density, c_p is the specific heat capacity, ΔT is the temperature rise and α is the current plastic strain. β_{int} is the integral Taylor-Quinney factor [49], which expresses the fraction of the plastic strain energy density converted into heat.

4.3 Calibration of the Material constitutive strength parameters

The material plasticity parameters were estimated using the experimental dataset and were then optimized using the LS-OPT tool to reproduce accurately the dynamic response and strain localisation observed during the experiments. The optimisation process followed the following steps:

(a) the parameters A, B and n were determined from the quasi-static dataset.

Journal of Applied Mechanics. Received August 11, 2022;
Accepted manuscript posted October 26, 2022. doi:10.1115/1.4056136

(b) the parameter C was determined from the measured high strain rate data.

(c) m was selected from the available literature concerning the material under investigation

(d) LS-OPT was used to optimize C and m for different loading cases such as quasi-static, pre-strained high rate, and high-rate monotonic experiments.

It is paramount to identify the set of material parameters able to reproduce the mechanical response obtained in all loading cases to carry out a detailed investigation on the stress state during strain localisation. An optimization approach known as sequential response surface method (SRSM) was used together with LS-OPT®, an analysis package easy to interface with the LS-DYNA pre and post processing tools. This has become a popular approach for the identification of the material parameters in nonlinear dynamic simulations [50, 51]. The employed method minimises the distance between the experimental data and the material model, and generates a new response surface at each iteration.

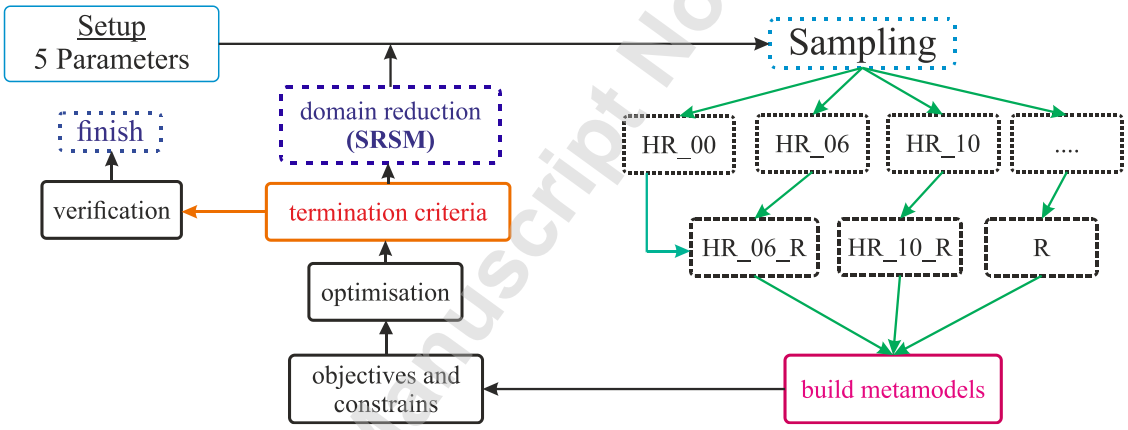

Figure 12: schematic layout of the LS-OPT optimisation interface used for various pre-straining loading cases.

Figure 12 presents the layout of the LS-OPT interface. The numerical models associated to each pre-strain loading case (monotonic, 6 %, 10% and 14% pre-strain, labelled in Figure 12 as HR_00, HR_06, HR_10 and HR_14.) were converted into meta-models for optimisation and sensitivity analysis. An appropriate function is used to define objectives and constraints to iteratively optimise the material parameters with respect to all experimental measurements. The engineering stress-strain characteristics determined from experiments for each loading cases were used as the optimisation goals. The final set of material parameters from LSOPT is tabulated in Table 4.

Journal of Applied Mechanics. Received August 11, 2022;
Accepted manuscript posted October 26, 2022. doi:10.1115/1.4056136

Table 4: Calibrated JC material model constants for Ti6Al-4V.

Material	Ti-6Al-4V	Source
Density ρ_0 $\left(\frac{kg}{m^3}\right)$	4419	[52]
Young's modulus (GPa)	110	
Specific heat, C_p $\left(\frac{J}{Kg \cdot K}\right)$	526	[52]
J-C strength model		
Shear modulus G (GPa)	44	[52]
Yield strength A (GPa)	0.908	Obtained from QS LSOPT
Hardening constant B (GPa)	0.735	
Hardening exponent n	0.567	
Strain rate constant C	0.0274	Obtained from Dynamic tests
Thermal exponent m	0.599	
Reference strain rate, $\dot{\varepsilon}_0$ (s^{-1})	0.0008	Experimental conditions
Reference temperature $t_0(K)$	293	
Melting temperature tm (K)	1875	[53]
Taylor-Quinney	0.85	Optimized using simulation

The first assessment of the fidelity of the numerical simulations is performed against the high-rate and quasi static experiments on pristine samples. The outcome is presented in Figure 13 (a). It is evident that the numerical analyses are able to predict the engineering stress-strain behaviour quite well for both loading rates. Figure 13 (b) illustrates the numerical outcome obtained after the optimisation carried out in LS-OPT and presents a comparison between experimental and numerical results for the various pre-strain levels. The optimization process

Journal of Applied Mechanics. Received August 11, 2022;
Accepted manuscript posted October 26, 2022. doi:10.1115/1.4056136

481 resulted in very good predictions for all cases, i.e. monotonic and pre-strain levels equal to 6%,
482 10% and 14%. When pre-strained specimens were tested at high rate, the data indicated a rise
483 in the yield stress in the region of 100 - 150 MPa compared to the pristine response. A similar
484 outcome from the simulations confirms the validity of the numerical set-up.

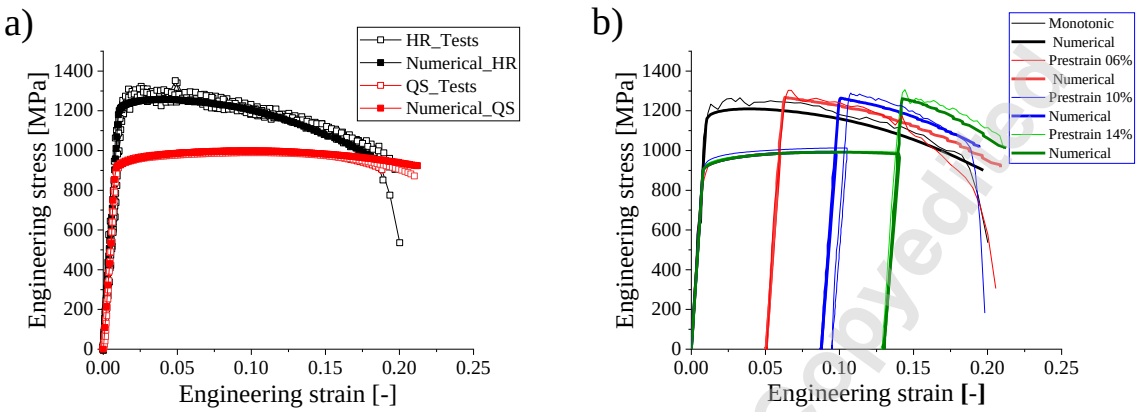

485
486 Figure 13: comparison of numerical predictions and experimental results on Ti6Al4V samples: (a) monotonic response and
487 (b) predictions of monotonic and pre-strain experiments after LS-OPT optimization.

488 Additionally, to investigate the influence of the strain history on the stress state around the
489 necked region, it is important to examine the local behaviour of the numerically produced
490 datasets. Figure 14 presents a detailed comparison between the numerical and experimental
491 diameter contractions. The predicted diameter evolutions show a very good agreement with the
492 experimental dataset, confirming the validity of the numerical framework. It is therefore
493 possible to use these simulations as a reliable way to study and compare the stress state
494 evolution in each loading case.

Journal of Applied Mechanics. Received August 11, 2022;
Accepted manuscript posted October 26, 2022. doi:10.1115/1.4056136

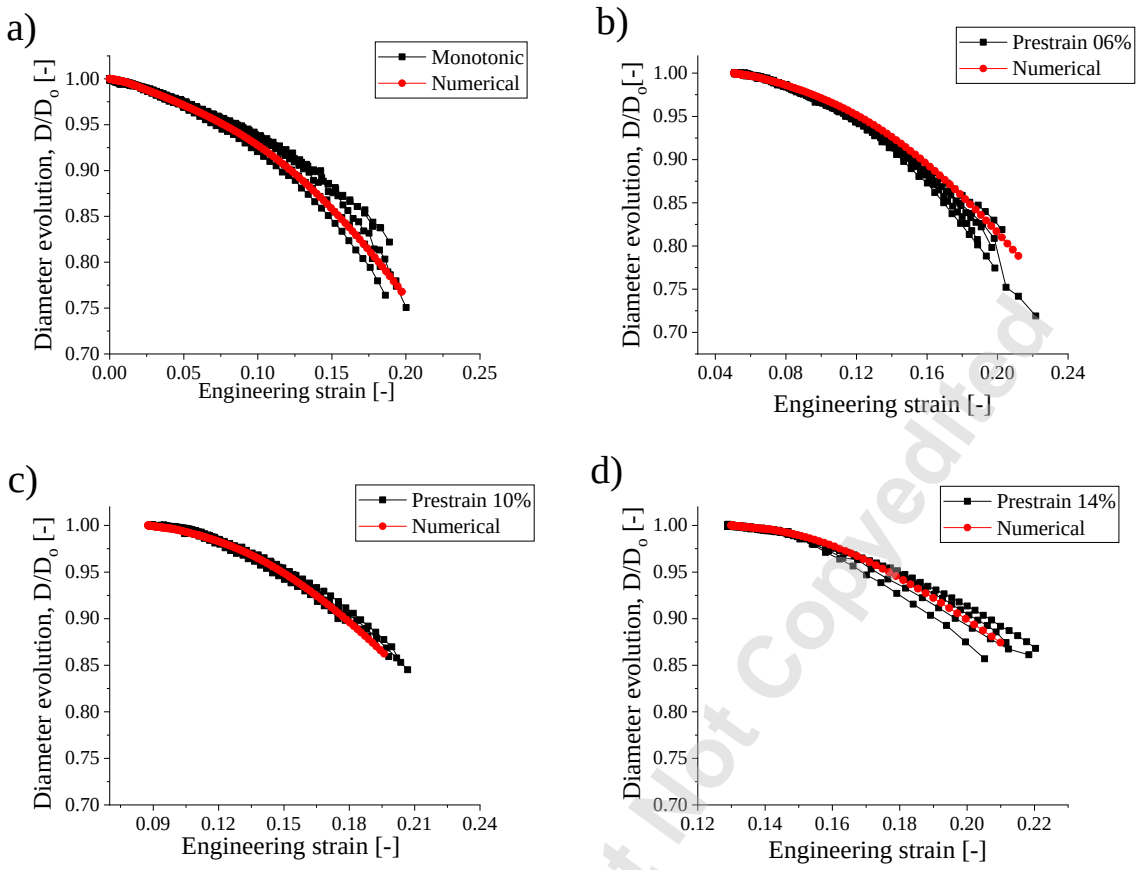

Figure 14: comparison of experimental data and numerical predictions of the diameter evolution for monotonic and pre-strained loading cases.

As both the diameter evolution in the necking area and engineering curves are in very good agreement with experimental data, the numerical simulations are believed to be accurate and suitable to investigate the stress triaxiality within the specimen, as detailed in the following section.

5. Stress state in the necked regions and consideration on stress triaxiality

Before the onset of necking, the deformation of the specimen is uniform and the mechanical characteristic of the sample can be estimated easily. After the inception of necking, deformations are no longer uniform, and strain localisation exacerbate while the force acting on the sample decreases, until failure. In this phase deformations localise around the minimum cross section and cannot be related anymore to the gauge length. A complete stress strain curve can only be obtained if the neck area is monitored during the test. Additionally, the regions of the sample near the neck constrain the reduction of the minimum cross section, and a triaxial

stress state develops in this region. As a result the equations used for the determination of true stress and true strain cannot be used to compute the equivalent stress-strain response. In this work the effect of the pre-strain on the evolution of stress triaxiality during dynamic tensile loading is investigated and compared for various levels of strain history. Moreover, correction methods such as Bridgman, Gromada and MLR are employed to assess their capability for the studied loading cases. The validated numerical results are used to examine the stress state within the necked zone and the influence of the pre-straining on the stress distributions.

5.1 Analysis and comparison of the stress states within the necking area.

The estimation of the average axial stresses (σ_x) from experimental measurements is not sufficient to detail the overall stress state during dynamic strain localization. After the onset of necking, the deformation does not remain uniform, resulting in a non-uniform distribution of stresses around the necked zone. In this area, non-uniform radial (σ_r) and hoop stresses (σ_h) become significant and even the axial stresses (σ_x) depart from uniformity. This is shown clearly in Figure 15 (a), where the distribution of the axial stresses (σ_x) along the normalised radial coordinate $\left(\frac{r}{a}\right)$ is presented for a state of deformation corresponding to ε_{eng} equal to 15%. It can be inferred, from Figure 15 (a), that, σ_x varies from 1615 MPa to 1280 MPa in the monotonic case, whereas it ranges from 1650 MPa to 1541 MPa for the 14% pre-strained experiment. The distributions of σ_x become flatter as the pre-strain level is increased. A similar trend is observed in the distribution of radial stresses σ_r, which is approximately analogous to the distribution of the hoop stresses σ_h. Figure 15 (b) shows that the variation of radial strains across the specimen cross section is more pronounced in the monotonic case and it gradually decreases for increasing levels of pre-strain. This clearly indicates the complexities posed by strain localisation in the experimental measurements of the equivalent stress σ_{eq}.

Journal of Applied Mechanics. Received August 11, 2022;
Accepted manuscript posted October 26, 2022. doi:10.1115/1.4056136

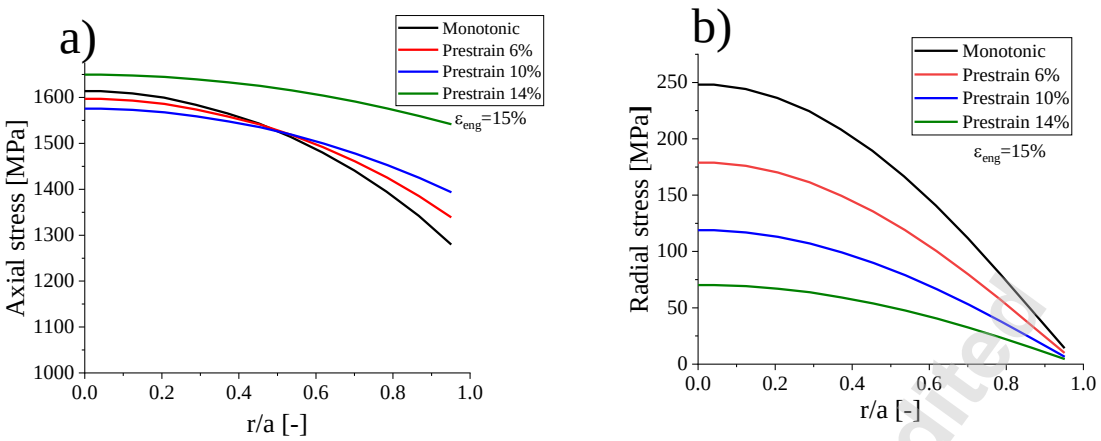

Figure 15: axial and radial stress distribution in the necking region for various pre-strain cases. The displayed distributions were obtained for a total engineering strain equal to 15%.

The different stress states in the necked section are further investigated comparing the distributions of axial, von Mises (σ_{eq}) and true stress (σ_{true}) when the engineering strain ε_{eng} in the sample is equal to 15%. The comparison is presented in Figure 16. It is noted that the true stress σ_{true} is the stress obtained using Eq. (6) and, therefore, is constant across the necked section. Conversely, axial and equivalent Mises stresses vary across the minimum cross section. The difference between von Mises stress and true stress is higher in the case of monotonic loading on pristine samples, and becomes smaller as the level of pre-strain increases. More in detail, this gap is approximately 71 MPa for high-rate monotonic loading and decreases to 24 MPa for a pre-strain of 14%. This trend is explained by the different amount of plastic work converted into adiabatic heating, gradually lower for increasing levels of pre-strain. The increase in temperature caused by adiabatic heating induces the neck to be more pronounced and, consequently, the triaxiality of the stress state to become more noticeable.

In essence, strain localisation causes the stress state to depart from uniaxial conditions, introducing non-uniform stress distributions and, in turn, a noticeable difference between the true stress σ_{true} (Eq.6) and the equivalent von Mises stress σ_{eq}. This difference becomes larger when the necking is very pronounced, as in the case of ductile metal alloys or significant adiabatic heating.

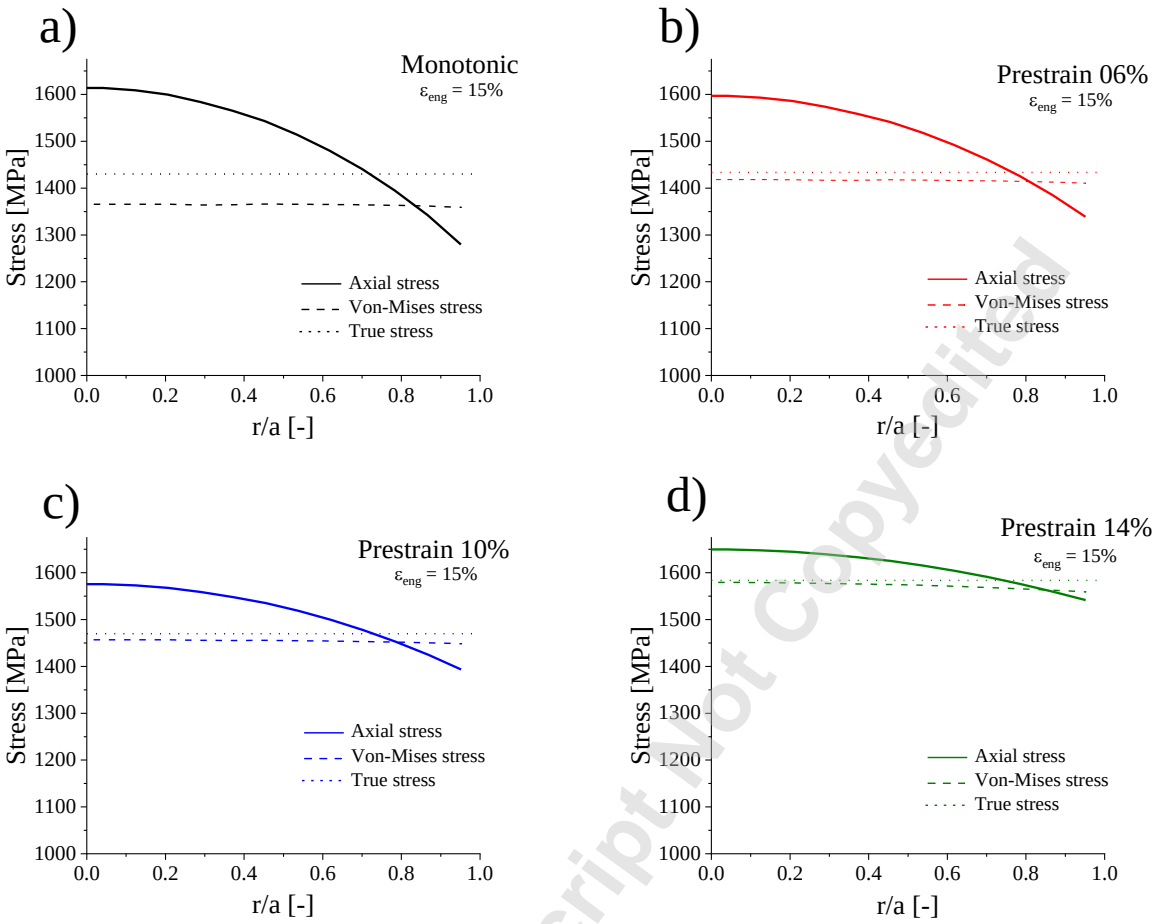

Figure 16:axial, true, and von Mises stress in the necked region during high-rate tensile loading on: a) pristine samples b) 6% pre-strained samples, c) 10% pre-strained samples and d) 14% pre-strained samples.

The characterisation of the mechanical behaviour of ductile alloys requires the conversion of σ_{true} to σ_{eq}. The literature reports various corrections to determine σ_{eq} from the experimentally measurable σ_{true}, such as the ones proposed by Bridgman, Gromada, and the recently developed MLR. The applicability of these solutions to high-rate experiments is assessed in the following section, where the numerical simulations detailed in section 4 are used to analyse each of the investigated loading cases.

5.2 Stress correction in post-necking tension of cylindrical specimen

This section details the different analytical corrections to convert true stress to equivalent stress.

5.2.1 Bridgman correction

Bridgman [29] proposed an analytical solution to correct the true stress to the equivalent stress in the post-necking regime. The method is applicable for axisymmetric specimens and isotropic materials and requires the continuous measurement of the minimum cross section radius and of the necking curvature radius. The Bridgman correction factor $\xi_{Bridgman}$ can be expressed as below:

$$\xi_{Bridgman} = \frac{\sigma_{true}}{\sigma_{eq}} = \left(1 + \frac{2R}{a}\right) Ln\left(1 + \frac{a}{2R}\right) \quad (10)$$

Where a is the current minimum cross section radius and R is the radius of curvature of the necking profile. The method is based on the hypothesis of volume conservation in the plastic regime and on the assumptions that strains are constant in the minimum cross section. Its error is reported to range between 5% and 15%, although it requires considerable effort to determine the radius of curvature of the necking profile [33]. In another study [32, 35] Gromada et al. conducted a numerical analysis and reported an inaccuracy of 10% for cases of ideal plasticity. Similar findings were reported by Needleman [54], who reported that the formula is accurate only at the early stages of necking. Experiments and modelling on SAE steel [55] indicated that the Bridgman correction may be inaccurate at large plastic strains. Muratha et al. [37] showed, by means of numerical analysis, that the flow stresses obtained using the Bridgman correction are higher than those obtained by inverse modelling. Gromada et al. [36] conducted a detailed investigation on each of the assumptions adopted by Brigdman and proposed two alternative formulations of the correction factor.

5.2.2 Gromada correction

Gromada et al. [36] adopted a semi-analytical approach to study the stress state in the necking region and correct for stress triaxiality in uniaxial tensile experiments. The detailed discussion about the formulation of this complex analytical solution, the adopted assumptions, boundary conditions and additional information can be found in [36]. Their study resulted in the correction formula below:

Journal of Applied Mechanics. Received August 11, 2022;
Accepted manuscript posted October 26, 2022. doi:10.1115/1.4056136

$$\eta_{Gromada} = \frac{\sigma_{eq}}{\sigma_{true}} = 1 - \frac{5\Lambda}{7(1+5\Lambda)} - \frac{2(1-6\Lambda)}{7(1+5\Lambda)} + \frac{2}{7} + \frac{30\Lambda(8\Lambda - \delta - 5\delta\Lambda)}{49\delta(1+5\Lambda)^2} + \frac{3(8\Lambda-\delta-5\delta\Lambda)}{7\delta(1+5\Lambda)}\left(\frac{2(1-6\Lambda)}{7(1+5\Lambda)} - \frac{2}{7} - \frac{30\Lambda(8\Lambda - \delta - 5\delta\Lambda)}{49\delta(1+5\Lambda)^2}\right) ln\left|1 + \frac{7\delta(1+5\Lambda)}{3(8\Lambda-\delta-5\delta\Lambda)}\right| \quad (11)$$

Where $\delta = \frac{a}{R}$ is ratio of the current radius of minimum cross-section to the radius of curvature of the necking profile R, while Λ is determined as $\Lambda = 1 - \frac{a_0}{a}$, where a_0 is the initial radius. Similarly to the Bridgman correction, the above formulation requires the determination of the curvature radius of the necked section. Therefore, two distinct analytical equations were employed for the calculation of $\frac{a}{R}$ as a function of the difference between the engineering plastic strain ε_p, and the ultimate engineering plastic strain ε_{Pmax} corresponding to the onset of necking. The first equation was developed by Le Roy in [55] and it is as follows:

$$\frac{a}{R} = 1.1(\varepsilon_p - \varepsilon_{Pmax}) \quad (13)$$

This ratio follows the linear trend observed experimentally at large strains but present some limitations. Therefore, it has been further improved by Lu et al. [56] to take into account of the nonlinear transition detected between the onset of necking and pronounced strain localisation. The equation proposed by Lu et al. [56] includes an exponential term and it is as follows:

$$\frac{a}{R} = k_1(\varepsilon_p - \varepsilon_{Pmax}) - k_2\left(1 - exp\left(-\frac{k_1}{k_2}(\varepsilon_p - \varepsilon_{Pmax})\right)\right) \quad (14)$$

5.2.3 MLR correction

Recently, Mirone, La Rosa et al. [31, 33] developed a convenient material independent correction to convert the true stress to equivalent stress. This third order polynomial equation was successfully tested for various materials and proved to predict accurately the equivalent stress of metallic ductile alloys. The MLR polynomial is expressed as follows:

$$\frac{\sigma_{eq\_avg}}{\sigma_{true}} = MLR(\varepsilon_{eq} - \varepsilon_N) \quad (15)$$

Journal of Applied Mechanics. Received August 11, 2022;
Accepted manuscript posted October 26, 2022. doi:10.1115/1.4056136

$$MLR(\varepsilon_{eq} - \varepsilon_N) = 1 - 0.6058 \cdot (\varepsilon_{eq} - \varepsilon_N)^2 + 0.6317 \cdot (\varepsilon_{eq} - \varepsilon_N)^3 - 0.2107 \cdot (\varepsilon_{eq} - \varepsilon_N)^4 \quad (16)$$

Here, ε_N is the true strain at the initiation of necking, ε_{eq} is the true current equivalent strain and σ_{eq_avg} is the true equivalent stress averaged over the minimum cross section.

6. Results and Discussion

The effectiveness of the above-detailed analytical corrections was evaluated comparing their predictions against the results extracted from the numerical simulations detailed in section 4. Both the Bridgman and the Gromada formulations require the determination of the ratio $\left(\frac{a}{R}\right)$. This was determined extracting the necking radius and necking profile from the numerical simulations when using the classic Bridgman formulation (*Brigman_C* in Figure 17 and Figure 18). Differently, the Le Roy (13) and Feng Lu (14) equations were used for the Gromada and the additional Bridgman corrections (*Gromada_LE, Gromada_FENG, Bridgman_LE* and *Bridgman*_FENG in Figure 17 and Figure 18). Figure 17 (a) presents an overall comparison of the predictions obtained using the various analytical corrections for quasi-static loading. The classic Bridgman and polynomial MLR follow the numerical trend of $\frac{\sigma_{eq}}{\sigma_{true}}$ (*Ratio_NUM_QS* in Figure 17 (a)) quite closely at low strains but start to diverge once the necking becomes pronounced. The predictions obtained using the Bridgman and Gromada corrections in conjunction with the Le Roy [57] equation present a linear trend, which is incongruous with the material response. The Bridgman and Gromada correction in conjunction with the Lu et al. [56] equation, indicate non-linear transitions which are close to the actual material behaviour, but certain discrepancies still exist. During dynamic loading conditions, necking initiates at an early stage compared to quasi-static loading. Figure 17 (b) presents the comparison of the predictions obtained using the various analytical corrections for high-rate monotonic loading. The classic Bridgman correction is unable to follow the numerically predicted material behaviour (*Ratio_NUM_HR* in Figure 17 (b)), with errors up to 8.3% as the strain localises, while the MLR displays a maximum error equal to 6.5%. Similar performances were obtained by the Gromada and Bridgman corrections associated with the Feng Lu equation. The determination of the Gromada and Bridgman corrections obtained using the Le Roy equation

Journal of Applied Mechanics. Received August 11, 2022;
Accepted manuscript posted October 26, 2022. doi:10.1115/1.4056136

637 yield predictions that are closer to the modelled material behaviour but display a trend that
638 appears dissimilar from the trend shown by the numerical results.

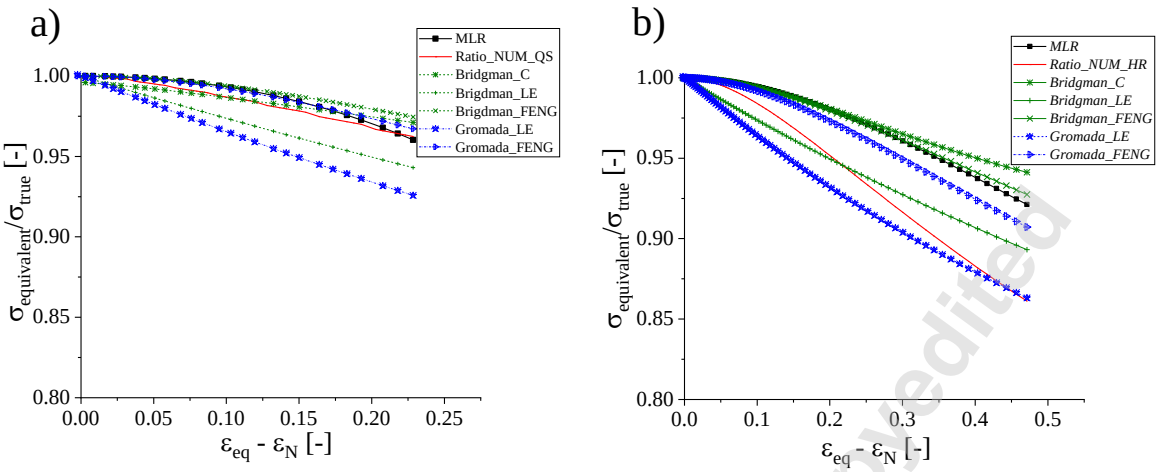

639
640 Figure 17: $\frac{\sigma_{eq}}{\sigma_{true}}$ ratio :comparison of various analytical solutions for (a) quasi-static and (b) high-rate loading conditions.

641 Same analytical formulations and comparisons were used to assess the corrections for dynamic
642 tensile loading on samples characterised by different levels of pre-strain (Figure 18 a, b and c).
643 For a pre-strain equal to 6%, the discrepancy between the classic Bridgman correction and the
644 numerically predicted material behaviour reaches 8.6% as strain localises. The other
645 corrections attain slightly better results, however the analytical corrections still present
646 significant discrepancies with respect to the modelled material behaviour. It is also noted that
647 the estimation of the ratio (a/R) using Eq. 14 makes the trend of the predicted $\frac{\sigma_{eq}}{\sigma_{true}}$ ratio non-
648 linear, which is closer to the real material response. For higher pre-strains, such as 14%, the
649 ratio between the von Mises and the true stress becomes less significant and the predictions
650 provided by the Bridgman and Gromada corrections using the Le Roy equation produce decent
651 results. However, divergences, both in terms of numerical values and trends are still present.
652
653

Journal of Applied Mechanics. Received August 11, 2022;
Accepted manuscript posted October 26, 2022. doi:10.1115/1.4056136

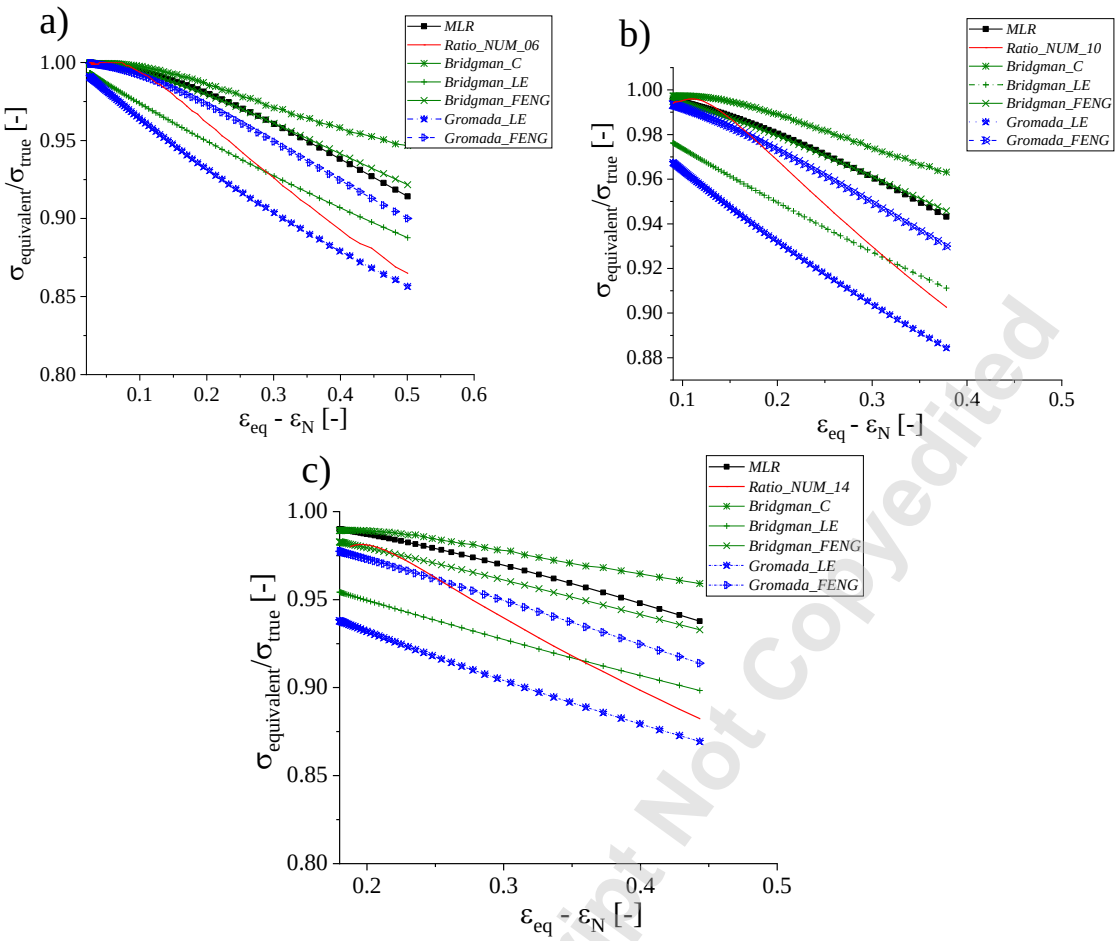

Figure 18: $\frac{\sigma_{eq}}{\sigma_{true}}$ ratio: comparison of various analytical solutions for dynamic tensile loading on samples characterised by different levels of pre-strain: (a) 06%, (b) 10% and (c) 14%.

The classical Bridgman and MLR formulations predict the ratio between equivalent and true stress quite well in quasi-static loading conditions. However, the different analytical corrections analysed in this study present limitations when applied to dynamic tensile loading on pristine and pre-strained samples, as necking becomes more pronounced and affected by adiabatic heating. None of the reviewed analytical formulations account for the heat generated during dynamic strain localization and this appears to be one of the contributing factors to the reduction of the ratio between von Mises and true stress. As the analytical correction formulas examined in this study appear to introduce some inaccuracies in the prediction of the equivalent stress for dynamic loading cases, the polynomial MLR equation was extended to account for adiabatic heating and improve its accuracy for dynamic loading conditions. The MLR correction was chosen as the baseline because of its accuracy and relatively easy

implementation when compared to the Bridgman and Gromada equations. The original MLR formulation was amended adding an exponential term accounting for the heat generated during high-rate deformation, including details of the Taylor Quinney coefficient and the specific heat of the material under investigation. An additional term considering the strain history in the sample is also included in the formulation. The extended formulation is as follows:

Quasi-static loading: $\frac{\sigma_{Eq\_avg}}{\sigma_{True}} = MLR(\varepsilon_{eq} - \varepsilon_N)$

High-rate loading: $\frac{\sigma_{Eq\_avg}}{\sigma_{True}} = DYN\_MLR(\varepsilon_{eq} - \varepsilon_N)$ (19)

$$MLR = 1 - 0.6058 \cdot (\varepsilon_{eq} - \varepsilon_N)^2 + 0.6317 \cdot (\varepsilon_{eq} - \varepsilon_N)^3 - 0.2107 \cdot (\varepsilon_{eq} - \varepsilon_N)^4$$

$$DYN\_MLR = (1 + b \cdot prestrain\ level) \cdot exp^{\left(-\frac{\eta}{C_P \cdot \rho}\right) \cdot a \cdot (\varepsilon_{eq} - \varepsilon_N)} \cdot MLR \quad (20)$$

Where η is the Taylor-Quinney coefficient of the material, C_p its specific heat, ρ its density, *prestrain* is the level of pre-strain in the material prior to dynamic deformation and *a* and *b* are constant to be determined via least square optimization. The values of the above physical properties for Ti6Al4V are reported in Table 4. The corresponding constants *a* and *b,* are 4.092×10^5 and 0.1669, respectively. Figure 19 illustrates the prediction of the ratio between the equivalent stress and true stress obtained using the extended MLR equation and the constants reported in Table 4. It is evident that the extended MLR correction is in excellent agreement with the results obtained using the optimised numerical simulations, for all levels of pre-strain. It is worth emphasising that the extended MLR formulation requires the use of different thermal properties and the determination of the corresponding constants *a* and *b* for different metals and metal alloys. However, it is reasonable to believe that the extended MLR formulation, in conjunction with the constants detailed in Table **4**: Calibrated JC material model constants for Ti6Al-4V.Table 4, provides an accurate prediction of the ratio $\frac{\sigma_{eq}}{\sigma_{true}}$ for titanium and titanium alloys as these are characterised by similar thermal properties as Ti6Al4V.

The veracity of the above consideration was verified by comparing the ratio $\frac{\sigma_{eq}}{\sigma_{true}}$ provided by the proposed formulation with the results obtained from monotonic experiments on Ti3Al2.5V conducted at strain rates included between 12 s^{-1} and 2700 s^{-1}, and their corresponding numerical simulations [58]. The outcome of this comparison is displayed in Figure 20. It is evident that, although the ratio $\frac{\sigma_{eq}}{\sigma_{true}}$ appears to follow for this material a different trend,

Journal of Applied Mechanics. Received August 11, 2022;
Accepted manuscript posted October 26, 2022. doi:10.1115/1.4056136

characterised by a substantially linear dependence on the post-necking plastic strain, the extended MLR formulation (Equation (20)) yields a more than satisfactory prediction of the ratio between von Mises and true stress.

The accuracy of the proposed modified MLR correction is assessed quantitatively for various values of post-necking strain in Table 5. The relative error of the proposed correction is below 3% for all examined cases, with a maximum error equal to 2.51%.

Table 5: relative error of the dynamic MLR correction at different values of post-necking strain.

$\varepsilon_{eq} - \varepsilon_N$	0.05	0.1	0.15	0.2	0.25	0.3	0.35
$ERR_{DYNMLR\text{-}Ti6Al4V\ SR2000}$	0.43%	0.42%	0.23%	0.00%	0.19%	0.29%	0.28%
$ERR_{DYNMLR\text{-}Ti3AL2.5V\ SR12}$	0.75%	1.37%	1.77%	1.95%	1.96%	1.87%	1.39%
$ERR_{DYNMLR\text{-}Ti3AL2.5V\ SR1200}$	0.49%	1.10%	1.66%	2.02%	2.28%	2.51%	1.92%
$ERR_{DYNMLR\text{-}Ti3AL2.5V\ SR2700}$	0.41%	1.04%	1.53%	2.04%	2.30%	2.42%	2.40%

The above results support the validity of the proposed correction for different titanium alloys and its applicability to the wide range of strain rates whereby nearly adiabatic heating conditions can be assumed.

Journal of Applied Mechanics. Received August 11, 2022;
Accepted manuscript posted October 26, 2022. doi:10.1115/1.4056136

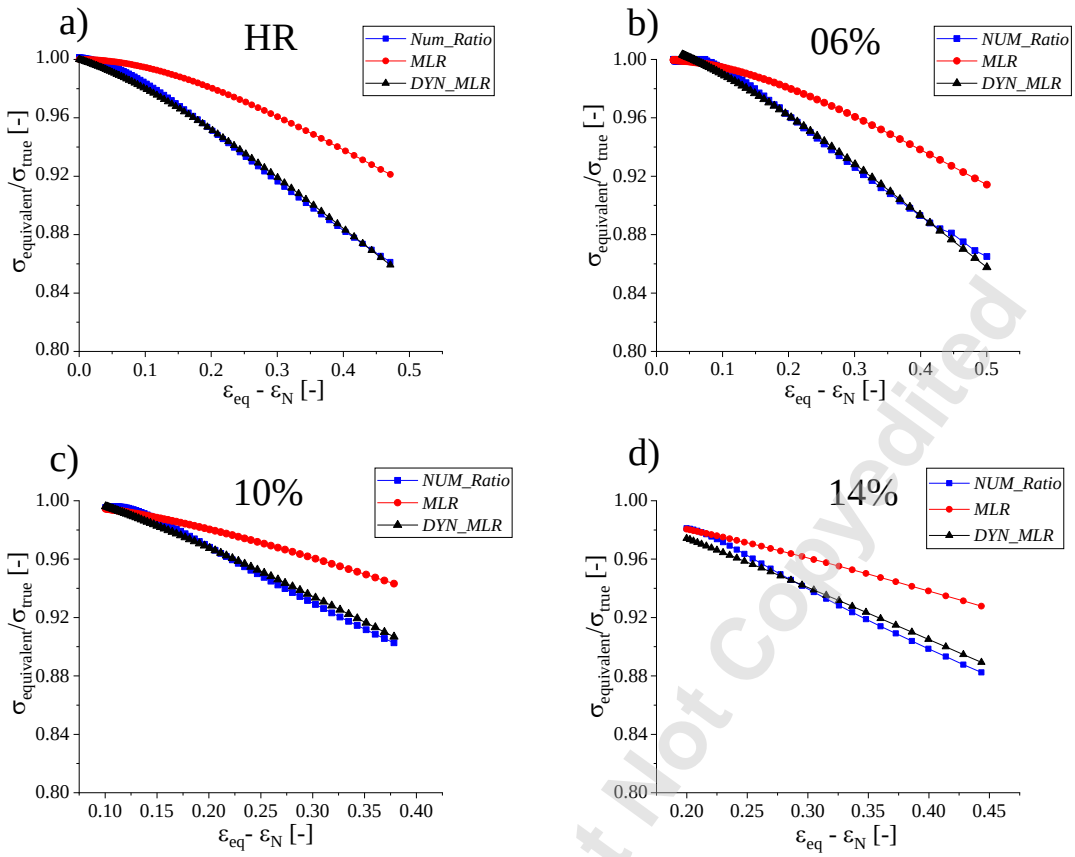

Figure 19: $\frac{\sigma_{eq}}{\sigma_{true}}$ratio: Predictions obtained using the extended MLR correction for high-rate tensile loading on: a) pristine samples b) 6% pre-strained samples, c) 10% pre-strained samples and d) 14% pre-strained samples.

Journal of Applied Mechanics. Received August 11, 2022;
Accepted manuscript posted October 26, 2022. doi:10.1115/1.4056136

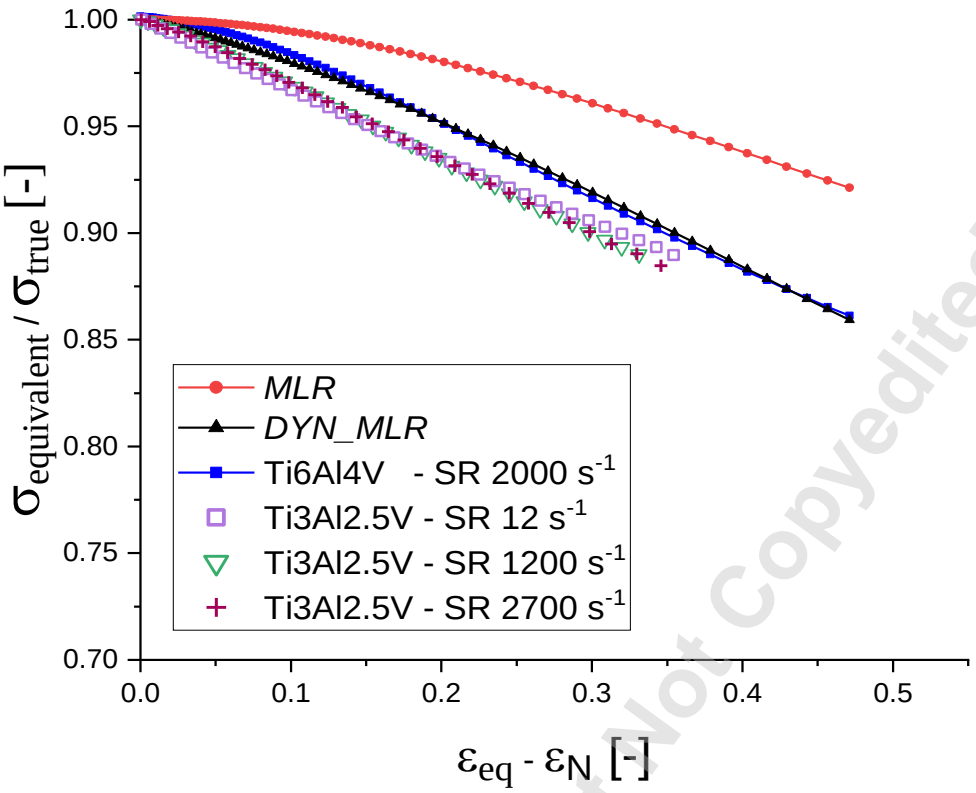

Figure 20: accuracy of the predictions obtained using the extended MLR correction with respect to experiments conducted on Ti6Al4V and Ti3Al2.5V at different strain rates.

7. Summary and conclusions

The present investigation assesses the effect of strain history on dynamic strain localisation and stress state during dynamic tensile loading experiments on Ti6Al4V. The outcome of the research herein presented can be summarised as follows:

- A series of dynamic tensile experiments on Ti6Al4V samples characterised by different levels of pre-strain were conducted. The evolution of the necking diameter and local strain rate was analysed and compared via image analysis of high speed camera footage.
- The temperature increase caused by adiabatic heating during dynamic loading was measured by means of high speed thermal imaging equipment.
- Numerical simulations able to reproduce accurately global and local thermo-mechanical variables were calibrated to analyse the stress state within the necking section of the samples. The stress state of samples of different pre-strain levels was analysed. The ratio between the Equivalent Mises stress and the average axial true stress

during deformation was determined for all examined experiments. The effectiveness of analytical corrections such as Bridgman, Gromada and MLR polynomial were assessed and compared. The results highlighted that the stress state in the necking area of the samples is affected by adiabatic heating and that none of the existing formulations was able to account for its influence.

- The MLR polynomial correction was amended to take into account for the temperature rise during dynamic loading. The proposed correction includes two additional constants (*a* and *b*) that depend on the thermal properties of considered material. It is worth emphasising that these are not material independent but need to be determined for different classes of alloys.
- The validity of the extended MLR correction herein proposed and of the constants reported in Table 4 was further assessed considering a series of monotonic experiments conducted on 3Al2.5V. The obtained results support the validity of the formulation for different titanium alloys and its applicability to a wide range of dynamic strain rates.

Further studies will focus on the application of the proposed analytical expression to high rate tensile experiments on different metal alloys.

Acknowledgement

The authors would like to thank Rolls-Royce plc and the EPSRC for the support under the Prosperity Partnership Grant\Cornerstone: Mechanical Engineering Science to Enable Aero Propulsion Futures, Grant Ref: EP/R004951/1.
The authors would also like to thank Mr Stuart Carter, Mr Jeffrey Fullerton, Mr Peter Tantrum and Mr Derek Robinson for manufacturing the specimens and for the helpful suggestions, Mrs Karen Bamford for her continuous support and Dr Longhui Zhang for the useful technical discussions.

References

1. Tuninetti, V. and A.M. Habraken, *Impact of anisotropy and viscosity to model the mechanical behavior of Ti–6Al–4V alloy.* Materials Science and Engineering: A, 2014. **605**: p. 39-50.

2. Gilles, G., et al., *Experimental characterization and elasto-plastic modeling of the quasi-static mechanical response of TA-6V at room temperature.* International Journal of Solids and Structures, 2011. **48**(9): p. 1277-1289.
3. Sneddon, S., et al., *Sensitivity of material failure to surface roughness: a study on titanium alloys Ti64 and Ti407.* Materials & Design, 2021. **200**: p. 109438.
4. Zhang, L., et al., *Rate dependent behaviour and dynamic strain localisation of three novel impact resilient titanium alloys: Experiments and modelling.* Materials Science and Engineering: A, 2020. **771**: p. 138552.
5. James, S., et al. *Timetal® 407: A titanium alloy to enable cost reduction*. in *Proceedings of the 13th world conference on titanium*. 2016. Wiley Online Library.
6. Davey, W., et al., *Fatigue Performance of the Novel Titanium Alloy Timetal 407.* MATEC Web Conf., 2018. **165**: p. 04001.
7. Mirone, G., *The dynamic effect of necking in Hopkinson bar tension tests.* Mechanics of Materials, 2013. **58**: p. 84-96.
8. Mirone, G., D. Corallo, and R. Barbagallo, *Experimental issues in tensile Hopkinson bar testing and a model of dynamic hardening.* International Journal of Impact Engineering, 2017. **103**: p. 180-194.
9. GRAY III, G.T., *Classic split Hopkinson pressure bar testing.* 2000(In: Kuhn H, Medlin D (eds) ASM Handbook Vol 8: mechanical testing and evaluation. Materials Park, OH, ASM International): p. 462-476.
10. Arthington, M.R., C.R. Siviour, and N. Petrinic, *Improved materials characterisation through the application of geometry reconstruction to quasi-static and high-strain-rate tension tests.* International Journal of Impact Engineering, 2012. **46**: p. 86-96.
11. Kapoor, R. and S. Nemat-Nasser, *Determination of temperature rise during high strain rate deformation.* Mechanics of Materials, 1998. **27**(1): p. 1-12.
12. Macdougall, D. and J.J. Harding, *The measurement of specimen surface temperature in high-speed tension and torsion tests.* International Journal of Impact Engineering, 1998. **21**: p. 473-488.
13. Macdougall, D., *Determination of the plastic work converted to heat using radiometry.* Experimental Mechanics, 2000. **40**(3): p. 298-306.
14. Noble, J.P. and J. Harding, *Temperature measurement in the tensile Hopkinson bar test.* Measurement Science and Technology, 1994. **5**(9): p. 1163-1171.
15. Ranc, N., et al., *Temperature field measurement in titanium alloy during high strain rate loading—Adiabatic shear bands phenomenon.* Mechanics of Materials, 2008. **40**(4): p. 255-270.
16. Soares, G.C., N.I. Vázquez-Fernández, and M. Hokka, *9 - Simultaneous full-field strain and temperature measurements in high strain rate testing*, in *Advances in Experimental Impact Mechanics*, B. Song, Editor. 2022, Elsevier. p. 255-285.
17. Varga, J. and O.T. Kingstedt, *An investigation of the plastic work to heat conversion of wrought and laser powder bed fusion manufactured Inconel 718.* Additive Manufacturing, 2021. **46**: p. 102179.
18. Soares, G. and M. Hokka, *The Taylor–Quinney coefficients and strain hardening of commercially pure titanium, iron, copper, and tin in high rate compression.* International Journal of Impact Engineering, 2021: p. 103940.
19. Vazquez-Fernandez, N.I., et al., *Adiabatic Heating of Austenitic Stainless Steels at Different Strain Rates.* Journal of Dynamic Behavior of Materials, 2019. **5**(3): p. 221-229.

20. Shamchi, S.P., et al., *Thermomechanical characterization of Alclad AA2024-T3 aluminum alloy using split Hopkinson tension bar.* Mechanics of Materials, 2019. **139**: p. 103198.
21. Rittel, D., L. Zhang, and S. Osovski, *The dependence of the Taylor–Quinney coefficient on the dynamic loading mode.* Journal of the Mechanics and Physics of Solids, 2017. **107**: p. 96-114.
22. Zaera, R., J.A. Rodríguez-Martínez, and D. Rittel, *On the Taylor–Quinney coefficient in dynamically phase transforming materials. Application to 304 stainless steel.* International Journal of Plasticity, 2013. **40**: p. 185-201.
23. Mirone, G., R. Barbagallo, and F. Giudice, *Locking of the strain rate effect in Hopkinson bar testing of a mild steel.* International Journal of Impact Engineering, 2019. **130**: p. 97-112.
24. Li, W., et al., *In situ EBSD study of deformation behavior of primary α phase in a bimodal Ti-6Al-4V alloy during uniaxial tensile tests.* Materials Characterization, 2020. **163**: p. 110282.
25. Bodunrin, M.O., et al., *Hot working of Ti-6Al-4V with a complex initial microstructure.* International Journal of Material Forming, 2019. **12**(5): p. 857-874.
26. Momeni, A., S.M. Abbasi, and S. Sadeghpour, *A comparative study on the hot deformation behavior of Ti5Al5Mo5V3Cr and newly developed Ti4Al7Mo3V3Cr alloys.* Vacuum, 2019. **161**: p. 410-418.
27. Li, J., et al., *Effect of pre-strain on fatigue crack growth behavior for commercial pure titanium at ambient temperature.* International Journal of Fatigue, 2018. **117**: p. 27-38.
28. Lanning, D.B., T. Nicholas, and G.K. Haritos, *Effect of plastic prestrain on high cycle fatigue of Ti–6Al–4V.* Mechanics of Materials, 2002. **34**(2): p. 127-134.
29. Bridgman, P., *The stress distribution at the neck of a tension specimen.* Trans. Amer. Soc, 1944.
30. La Rosa, G., G. Mirone, and A. Risitano, *Effect of stress triaxiality corrected plastic flow on ductile damage evolution in the framework of continuum damage mechanics.* Engineering Fracture Mechanics, 2001. **68**(4): p. 417-434.
31. Mirone, G., *A new model for the elastoplastic characterization and the stress–strain determination on the necking section of a tensile specimen.* International Journal of Solids and Structures, 2004. **41**(13): p. 3545-3564.
32. Gromada, M., G. Mishuris, and A. Öchsner, *An attempt to improve the evaluation of mechanical material properties from the axisymmetric tensile test.* Israel Journal of Chemistry, 2007. **47**(3-4): p. 329-335.
33. Mirone, G., *Role of stress triaxiality in elastoplastic characterization and ductile failure prediction.* Engineering Fracture Mechanics, 2007. **74**(8): p. 1203-1221.
34. Bai, Y., X. Teng, and T. Wierzbicki, *On the Application of Stress Triaxiality Formula for Plane Strain Fracture Testing.* Journal of Engineering Materials and Technology, 2009. **131**(2).
35. Gromada, M., G. Mishuris, and A. Ochsner, *On the evaluation of mechanical properties from the axisymmetric tensile test.* Archives of Metallurgy and Materials, 2010. **55**(1): p. 295-300.
36. Gromada, M., G. Mishuris, and A. Öchsner, *Correction formulae for the stress distribution in round tensile specimens at neck presence*. 2011: Springer Science & Business Media.
37. Murata, M., Y. Yoshida, and T. Nishiwaki, *Stress correction method for flow stress*

identification by tensile test using notched round bar. Journal of Materials Processing Technology, 2018. **251**: p. 65-72.
38. Quino, G., et al., *Speckle patterns for DIC in challenging scenarios: rapid application and impact endurance.* Measurement Science and Technology, 2020. **32**(1): p. 015203.
39. Pan, B., Z. Lu, and H. Xie, *Mean intensity gradient: An effective global parameter for quality assessment of the speckle patterns used in digital image correlation.* Optics and Lasers in Engineering, 2010. **48**(4): p. 469-477.
40. Gerlach, R., C. Kettenbeil, and N. Petrinic, *A new split Hopkinson tensile bar design.* International Journal of Impact Engineering, 2012. **50**: p. 63-67.
41. Pantleon, W., D. Francke, and P. Klimanek, *Modelling adiabatic heating during high-speed deformation.* Computational Materials Science, 1996. **7**(1): p. 75-81.
42. Soares, G.C., et al., *Effects of adiabatic heating and strain rate on the dynamic response of a CoCrFeMnNi high-entropy alloy.* Journal of Dynamic Behavior of Materials, 2019. **5**(3): p. 320-330.
43. Che-Haron, C.H. and A. Jawaid, *The effect of machining on surface integrity of titanium alloy Ti–6% Al–4% V.* Journal of Materials Processing Technology, 2005. **166**(2): p. 188-192.
44. Duarte Filho, L.A. and A.M. Awruch, *Geometrically nonlinear static and dynamic analysis of shells and plates using the eight-node hexahedral element with one-point quadrature.* Finite Elements in Analysis and Design, 2004. **40**(11): p. 1297-1315.
45. Johnson, G.R. and W.H. Cook, *A constitutive model and data for metals subjected to large strains, high strain rates and high temperatures.*
46. Vázquez-Fernández, N.I., et al., *Uncoupling the effects of strain rate and adiabatic heating on strain induced martensitic phase transformations in a metastable austenitic steel.* Acta Materialia, 2019. **176**: p. 134-144.
47. Farren, W.S. and G.I. Taylor, *The heat developed during plastic extension of metals.* Proceedings of the Royal Society of London. Series A, Containing Papers of a Mathematical and Physical Character, 1925. **107**(743): p. 422-451.
48. Taylor, G.I. and H. Quinney, *The latent energy remaining in a metal after cold working.* Proceedings of the Royal Society of London. Series A, Containing Papers of a Mathematical and Physical Character, 1934. **143**(849): p. 307-326.
49. Rittel, D., *On the conversion of plastic work to heat during high strain rate deformation of glassy polymers.* Mechanics of Materials, 1999. **31**(2): p. 131-139.
50. Benson, D.J., et al. *On the application of LS-OPT to identify non-linear material models in LS-DYNA*. in *7th International LS-DYNA Users Conference, Dearborn, MI*. 2002.
51. Müllerschön, H., et al. *The identification of rate-dependent material properties in foams using LS-OPT*. in *3rd European LS-DYNA Users Conference, Paris, France*. 2001.
52. Williams, G.L.J.C., *Titanium*. 2003, Berlin: Springer.
53. Welsch, G., R. Boyer, and E. Collings, *Materials properties handbook: titanium alloys*. 1993: ASM international.
54. Needleman, A., *A numerical study of necking in circular cylindrical bar.* Journal of the Mechanics and Physics of Solids, 1972. **20**(2): p. 111-127.
55. Cabezas, E.E. and D.J. Celentano, *Experimental and numerical analysis of the tensile test using sheet specimens.* Finite Elements in Analysis and Design, 2004. **40**(5-6): p. 555-575.
56. Lu, F., T. Mánik, and B. Holmedal, *Stress corrections after necking using a two-parameter equation for the radius of curvature.* Journal of Applied Mechanics, 2021.

88(6).
57. Le Roy, G., et al., *A model of ductile fracture based on the nucleation and growth of voids.* Acta Metallurgica, 1981. **29**(8): p. 1509-1522.
58. Zhang, L., et al., *Strain rate and temperature dependent strain localization of a near α titanium alloy.* International Journal of Impact Engineering, 2020. **145**: p. 103676.